Advances in Materials Research, *Vol. 13, No. 6 (2024) 431-462*
https://doi.org/10.12989/amr.2024.13.6.431

Comparative study on the buckling analysis of exponential, power and sigmoidal sandwich FGM plates under hygro-thermal conditions

Aman Garg*[1,2], Mohamed-Ouejdi Belarbi[3,4], Li Li[2], H.D. Chalak[5], Abdelouahed Tounsi[6,7,8] and A.M. Zenkour[9,10]

[1]*State Key Laboratory of Intelligent Manufacturing Equipment and Technology, School of Mechanical Science and Engineering, Huazhong University of Science and Technology, Wuhan 430074, China*
[2]*Department of Multidisciplinary Engineering, The NorthCap University, Gurugram, Haryana, India – 122017*
[3]*Laboratoire de Recherche en Génie Civil, LRGC, Université de Biskra, B.P. 145, R.P. 07000, Biskra, Algeria*
[4]*Department of Civil Engineering, Lebanese American University, Byblos, Lebanon*
[5]*Department of Civil Engineering, National Institute of Technology Kurukshetra, Haryana, India – 136119*
[6]*Department of Civil and Environmental Engineering, King Fahd University of Petroleum &Minerals, 31261 Dhahran, Eastern Province, Saudi Arabia*
[7]*Material and Hydrology Laboratory, University of Sidi Bel Abbes, Faculty of Technology, Civil Engineering Department, 22000 Sidi Bel Abbes, Algeria*
[8]*YFL (Yonsei Frontier Lab), Yonsei University, Seoul, Korea*
[9]*Department of Mathematics, Faculty of Science, King Abdulaziz University, Jeddah, Saudi Arabia*
[10]*Department of Mathematics, Faculty of Science, Kafrelsheikh University, Kafrelsheikh, Egypt*

(*Received May 9, 2022, Revised August 10, 2024, Accepted September 19, 2024*)

Abstract. The buckling mode of failure is very common in case of plates, especially when their aspect ratio is large. In the present study, an endeavour has been made to carry out the hygro-thermal-induced buckling-based study of sandwich functionally graded (FG) plates made up of different material variation laws. A comparative study has been carried out between FGM plates made up of power, exponential and sigmoidal law using higher order zigzag theory. Nine-noded C-0 finite element has been used. It has been observed that the buckling behaviour of sandwich FGM plates under hygrothermal conditions is widely influenced by the geometry of the plate and the value of the law coefficient. Also, the nature of boundary condition widely affects the behavior of the plate.

Keywords: buckling; finite element; HOZT; hygro-thermal; stress continuity

1. Introduction

Functionally graded materials (FGMs) are taking the place of laminated composite materials because of problems of delamination (Garg and Chalak 2019), and stress channelling effects (Patni *et al*. 2018), etc. associated with laminates. In FGM materials, material property varies along a particular direction in the desired configuration. The Japanese invented FGMs during the 1990s, and

*Corresponding author, Ph.D., E-mail: amang321@gmail.com

http://www.techno-press.org/?journal=amr&subpage=5 ISSN: 2234-0912 (Print), 2234-179X (Online)

in a short span of 30 years, they are widely adopted for constructing various structures in the field of civil, aerospace, naval, automobile, etc. (Garg *et al*. 2021a, 2022a).

To predict the behaviour of sandwich FGM plates efficiently, several theories are available in the literature. The simplest theory available in the literature is the classical laminated theory (CLT) based upon the Euler- Bernoulli beam theory (Love 1888). However, this theory neglects transverse deformation effects and cannot predict the behaviour of structures efficiently (Garg and Chalak 2019, Bellifa *et al*. 2021, Hosseini *et al*. 2022). First-order shear deformation theory (FSDT) assumes a constant transverse displacement field across the thickness of the plate (Jalali *et al*. 2010, urpa and Shmatko 2020). Kiani and Elsami 2012 carried out a thermal-based buckling analysis of imperfect sandwich FGM plates resting upon elastic foundations. Thai *et al*. (2014) published analytical solutions for buckling analysis of sandwich FGM plates using FSDT. Kırlangıç and Akbaş 2021 carried out a dynamic analysis of FG beams using Timoshenko beam theory. Using FSDT, Kumar and Kattimani carried out the non-linear analysis of 2D FG shells. FSDT assumes a constant transverse displacement field across the thickness of the plate. This theory requires a shear correction factor whose actual value depends upon several parameters such as end condition, thickness scheme, etc. (Shariyat and Alipour 2013, Lim and Kim 2017, Garg and Chalak 2019). A continuum model was proposed by Alnujaie *et al*. 2021 for dynamic forced vibration analysis of porous, thick FG beams.

The next class of theory, called higher-order shear deformation theory (HSDT), expands the in-plane displacement field as higher-order variations concerning the plate's thickness coordinates (Nguyen 2021, Civalek *et al*. 2022). Several variations of HSDT are available in the literature depending upon the order and the way of expression, such as trigonometric (Fazzolari 2018, Tounsi *et al*. 2013, Belarbi *et al*. 2022), hyperbolic (Akavci 2016, Mahi *et al*. 2015), exponential (Osofero *et al*. 2016, Trinh *et al*. 2016) HSDTs, etc. The most common type of HSDT used is Reddy's HSDT. Zenkour and his co-authors (Zenkour 2005a, Zenkour and Sobhy 2010) carried out buckling analysis of power-law sandwich FGM plates using sinusoidal SDT (SPT), Reddy's SDT (HPT), and FSDT using Navier's solution under normal and thermal conditions. Wang and Shen 2011 and Shen and Li 2008 carried out a buckling analysis of sandwich FGM plates resting upon elastic foundation using HSDT under thermal conditions. Sobhy (2016) carried out a buckling analysis of sandwich FGM plates resting on Winkler–Pasternak elastic foundations under hygrothermal conditions. Meksi *et al*. (2019) used Navier's solution-based HSDT for the buckling analysis of sandwich FGM plates. Trinh *et al*. 2018 carried out a buckling analysis of sandwich FGM plates using state-space Levy's solution. Singh and Harsha (2019) carried out a buckling analysis of sandwich FGM plates resting on elastic foundations. Daikh and Zenkour 2019 employed HSDT for the buckling analysis of porous FGM plates. Barati and Zenkour 2019a, b employed HSDT for buckling analysis of FG nanobeams. Adhikari *et al*. 2020 used finite element (FE; 8 noded FE with 9 d.o.f. per node) based HOSDT for the buckling analysis of porous sandwich FGM plates, neglecting normal transverse stresses during formulation. Zenkour and Radwan (2019, 2020) carried out the buckling analysis of sandwich FGM plates resting on elastic foundations under hygrothermal conditions. Zenkour and his co-authors (Sobhy and Zenkour 2019, Zenkour and Aljadani 2019, 2020, Mashat and Zenkour 2020) carried out buckling analysis of FG plates and nanoplates (Sobhy and Zenkour 2019) containing piezoelectric layers using HSDT. Sahoo *et al*. employed finite element-based HSDT for thermal-based buckling analysis of FG plates. Using hyperbolic shear deformation theory, Bouazza and Zenkour (2020) carried out a buckling analysis of sandwich beams under hygro-thermo-mechanical loading. Al-Osta *et al*. (2021) studied the hygro-thermo-mechanical-based response of axially FG plates. Hadji and Tounsi (2021) carried out the analysis of porous FG sandwich plates. Higher-order

sandwich panel theory was improved by Soleimani-Javid *et al*. (2021) for vibration analysis of sandwich plates. Belarouci and Fekrar (2021) carried out the analysis of thick FG plates resting on elastic foundations using quasi-3D theory. Belkhodja *et al*. (2022) proposed five unknowns-based HSDT for buckling analysis of FGM plates. Al-Osta (2022a, b) carried out wave propagation analysis in defected exponentially graded plates. Cuong-Le *et al*. (2022a, b, c) carried out bending, vibration and buckling analysis of FG nanoplates using iso-geometric analysis. Zhang and Cao (2022) employed HSDT for predicting the vibration behavior of axially graded truncated conical nanoshells in the framework of nonlocal strain gradient theory. With the help of generalized SDT, Nguyen *et al*. (2022) studied the behaviour of floating plates in the framework of the finite element method.

Most of the available HSDTs assume a constant transverse displacement field across the plate's thickness or neglect normal transverse strains that cannot predict the behaviour of moderately thick and thick sandwich FGM plates efficiently (Brischetto 2009, Carrera *et al*. 2011, Garg *et al*. 2020a). Regarding the inclusion of zigzag effects and normal transverse strains, Carrera *et al*. (Carrera *et al*. 2011) stated, "Refinements of classical theories that include additional in-plane variables could result meaningless unless transverse normal strain effects are taken into account." Regarding the application of HSDT for analysis of sandwich FGM structures, Di Sciuva and co-authors (Iurlaro *et al*. 2014, Di Sciuva and Sorrenti 2021, Garg *et al*. 2022b) stated, "The Reddy's HSDT, typically used in literature to describe the behaviour of FGM structures, is not capable like the refined zigzag theories (RZT) to catch the distribution of local response for an orthotropic FGM sandwich plate." Thus, the inclusion of zigzag effects and normal transverse strain helps predict sandwich FGM plates' behaviour efficiently and accurately.

Neves *et al*. (2017) employed two different kinds of zigzag theories (HOZT), one considering transverse displacement field variation and the other considering constant transverse displacement field across the plate's thickness. It was observed that the formulation containing transverse displacement field variation gives more accurate results as compared to that considering the constant transverse displacement field. A similar type of result was also reported by Brischetto (2009). Natarajan and Manickam (2012) used Murakami's zigzag function-based HOZT for bending analysis of sandwich FGM plates using eight-noded serendipity quadrilateral shear flexible FE having 13 degrees of freedom per node. Fazzolari and Carrera (2014) and Fazzolari (2016) employed CUF for buckling analysis of sandwich FGM plates under thermal and normal conditions, respectively. Using the peridynamic differential operator (PDO), Dorduncu (2020) analyzed power-law and exponentially graded sandwich FGM plates with refined zigzag theory. Garg *et al*. (2020b, Garg *et al*. 2021b, c) carried out the analysis of sandwich FG beams and plates using finite element-based HOZT.

Novelty of present work

The literature survey shows that the hygrothermal-based buckling analysis of sandwich FGM plates using HOZT is not carried out. In the present work, hygro-thermal-based buckling analysis of sandwich FGM plates is carried out using recently proposed HOZT (Garg and Chalak 2021). Fourth-order and third-order variations of in-plane and transverse displacement fields are assumed. Zigzag effects are incorporated in both displacement fields using the unit Heaviside step function. Nine-noded C-0 Lagrangian FE having twelve degrees of freedom per node is used during analysis. The present formulation is free from the requirement of any penalty function or post-processing technique and hence is computationally efficient. The present formulation's effectiveness is demonstrated by comparing the present results with those available in the literature. Comparative hygrothermal-based buckling analysis for non-skew and skew sandwich FGM plates is carried out

between plates made up of different homogenization rules which are found to be absent in the literature. Equal rise or fall of temperature or moisture concentration across the plate's thickness is assumed during analysis. Several new results are also reported, especially for sigmoidal and exponential sandwich FGM plates, which will serve as the benchmark for future results.

2. Mathematical and material modeling

Consider a laminated plate of thickness h having $N^{(u)}$ number of upper layers and $N^{(l)}$ number of lower layers with respect to the plate's mid-plane, which is considered the reference plane during analysis. The in-plane and transverse displacement fields are chosen as:

$$U_{(x)} = u^{(0)} + z\varphi^{(x)} + z^2\mu^{(x)} + z^3\xi^{(x)} + z^4\psi^{(x)} + \sum_{i=1}^{N^{(u)}-1}\left(z - z_i^{(u)}\right)H\left(z - z_i^{(u)}\right)\Phi_i^{(x_u)} + \sum_{j=1}^{N^{(l)}-1}\left(z - z_j^{(l)}\right)H\left(-z + z_j^{(l)}\right)\Phi_j^{(x_l)} \tag{1}$$

$$U_{(y)} = v^{(0)} + z\varphi^{(y)} + z^2\mu^{(y)} + z^3\xi^{(y)} + z^4\psi^{(y)} + \sum_{i=1}^{N^{(u)}-1}\left(z - z_i^{(u)}\right)H\left(z - z_i^{(u)}\right)\Phi_i^{(y_u)} + \sum_{j=1}^{N^{(l)}-1}\left(z - z_j^{(l)}\right)H\left(-z + z_j^{(l)}\right)\Phi_j^{(y_l)} \tag{2}$$

$$U_{(z)} = w^{(0)} + z\varphi^{(z)} + z^2\mu^{(z)} + z^3\xi^{(z)} + \sum_{i=1}^{N^{(u)}-1}\left(z - z_i^{(u)}\right)H\left(z - z_i^{(u)}\right)\Phi_i^{(z_u)} + \sum_{j=1}^{N^{(l)}-1}\left(z - z_j^{(l)}\right)H\left(-z + z_j^{(l)}\right)\Phi_j^{(z_l)} \tag{3}$$

where, $u^{(0)}, v^{(0)}, w^{(0)}$ are the displacement of any point on the mid-plane about X- Y- and Z-axis, $\varphi^{(x)}, \varphi^{(y)}, \varphi^{(z)}$ are the rotation of the mid-plane about Y-, X- and Z-axis, respectively. $\mu^{(x)}, \mu^{(y)}, \mu^{(z)}, \xi^{(x)}, \xi^{(y)}, \xi^{(z)}, \psi^{(x)}, \psi^{(y)}$ represents higher-order unknowns. Φ denotes the slope of the ith/jth layer for the upper and lower layers. $H\left(z - z_i^{(u)}\right), H\left(-z + z_j^{(l)}\right)$ represents the Heaviside unit step function.

The stress-strain relationship for the k-th layer can be written as:

$$\{\sigma\} = [\bar{Q}]_k\left\{\varepsilon - \Delta T\{\alpha\} - \Delta c\{\beta\}\right\} \text{ or } \{\sigma\} = [\bar{Q}]_k\{\varepsilon_{net}\} \tag{4}$$

where, $\{\sigma\}$, $\{\varepsilon_{net}\} = \{\varepsilon\} - \{\varepsilon_{hygrothermal}\}$, $\{\alpha\}$, $\{\beta\}$, $[\bar{Q}]_k$, ΔT and Δc are the stress vector, strain vector, thermal expansion coefficient vector, moisture absorption coefficient vector, rigidity matrix for the *k-th* layer, change in temperature, and change in moisture concentration, respectively. Now utilizing the following conditions: $\sigma_{xz}^{h/2} = \sigma_{xz}^{-h/2} = \sigma_{yz}^{h/2} = \sigma_{yz}^{-h/2} = 0$; at interfaces: $\sigma_{xz}^{z} = \sigma_{xz}^{z+1}$, $\sigma_{yz}^{z} = \sigma_{yz}^{z+1}$, $\sigma_{zz}^{z} = \sigma_{zz}^{z+1}$; at $z = h/2$: $u = u^{(u)}, v = v^{(u)}, w = w^{(u)}$; at $z = -h/2$: $u =$

$u^{(l)}, v = v^{(l)}, w = w^{(l)}$.

With the help of the above-discussed conditions, the following unknowns $\mu^{(x)}$, $\mu^{(y)}$, $\mu^{(z)}$, $\xi^{(x)}$, $\xi^{(y)}$, $\psi^{(x)}$, $\psi^{(y)}$, $\Phi_i^{[x^{(u)}]}$, $\Phi_j^{[x^{(l)}]}$, $\Phi_i^{[y^{(u)}]}$, $\Phi_j^{[y^{(l)}]}$, $\Phi_i^{[z^{(u)}]}$, $\Phi_j^{[z^{(l)}]}$, $\frac{\partial w^{(u)}}{\partial x}$, $\frac{\partial w^{(u)}}{\partial y}$, $\frac{\partial w^{(l)}}{\partial x}$, $\frac{\partial w^{(l)}}{\partial y}$, can be written in terms of displacements $u^{(0)}$, $v^{(0)}$, $w^{(0)}$, $\varphi^{(x)}$, $\varphi^{(y)}$, $\varphi^{(z)}$, $u^{(u)}$, $v^{(u)}$, $w^{(u)}$, $u^{(l)}$, $v^{(l)}$, $w^{(l)}$ as:

$$\{M\} = [N]\{\Theta\} \tag{5}$$

where,

$$\{\Theta\} = \left\{u^{(0)}, v^{(0)}, w^{(0)}, \varphi^{(x)}, \varphi^{(y)}, \varphi^{(z)}, u^{(u)}, v^{(u)}, w^{(u)}, u^{(l)}, v^{(l)}, w^{(l)}\right\}^T$$

$$\{M\} = \mu^{(x)}, \mu^{(y)}, \mu^{(z)}, \xi^{(x)}, \xi^{(y)}, \xi^{(z)}, \psi^{(x)}, \psi^{(y)}, \Phi_1^{[x^{(u)}]}\ \Phi_2^{[x^{(u)}]}\ \ldots\ \Phi_{N^{(u)}-1}^{[x^{(u)}]}\ \Phi_1^{[x^{(l)}]}\ \Phi_2^{[x^{(l)}]}\ \ldots\ \Phi_{N^{(l)}-1}^{[x^{(l)}]}$$
$$\Phi_1^{[y^{(u)}]}\ \Phi_2^{[y^{(u)}]}\ \ldots\ \Phi_{N^{(u)}-1}^{[y^{(u)}]}\ \Phi_1^{[y^{(l)}]}\ \Phi_2^{[y^{(l)}]}\ \ldots\ \Phi_{N^{(l)}-1}^{[y^{(l)}]}\Phi_1^{[z^{(u)}]}\ \Phi_2^{[z^{(u)}]}\ \ldots\ \Phi_{N^{(l)}-1}^{[z^{(u)}]}\ \Phi_1^{[z^{(l)}]}\ \Phi_2^{[z^{(l)}]}\ \ldots\ \Phi_{N^{(l)}-1}^{[z^{(l)}]}$$
$$\frac{\partial w^{(u)}}{\partial x}, \frac{\partial w^{(l)}}{\partial x}, \frac{\partial w^{(u)}}{\partial y}, \frac{\partial w^{(l)}}{\partial y}\Big\}^T$$

and the elements of $[N]$ depends upon the property of the material of the layer.

Since the last four terms in the $\{M\}$ are the derivative terms and can be expressed easily in terms of displacement components $\{\Theta\}$, hence the problem associated with the C_1 continuity requirements can be avoided easily using the proposed model.

With the help of Eq. (5), the Eqs. (1)-(3) can be re-arranged as:

$$\begin{aligned} U_{(x)} = {} & a^{(1)}u^{(0)} + a^{(2)}v^{(0)} + a^{(3)}w^{(0)} + a^{(4)}\varphi^{(x)} + a^{(5)}\varphi^{(y)} + a^{(6)}\varphi^{(z)} + a^{(7)}u^{(u)} \\ & + a^{(8)}v^{(u)} + a^{(9)}w^{(u)} + a^{(10)}u^{(l)} + a^{(11)}v^{(l)} + a^{(12)}w^{(l)} \end{aligned} \tag{6}$$

$$\begin{aligned} U_{(y)} = {} & b^{(1)}u^{(0)} + b^{(2)}v^{(0)} + b^{(3)}w^{(0)} + b^{(4)}\varphi^{(x)} + b^{(5)}\varphi^{(y)} + b^{(6)}\varphi^{(z)} + b^{(7)}u^{(u)} \\ & + b^{(8)}v^{(u)} + b^{(9)}w^{(u)} + b^{(10)}u^{(l)} + b^{(11)}v^{(l)} + b^{(12)}w^{(l)} \end{aligned} \tag{7}$$

$$\begin{aligned} U_{(z)} = {} & c^{(1)}u^{(0)} + c^{(2)}v^{(0)} + c^{(3)}w^{(0)} + c^{(4)}\varphi^{(x)} + c^{(5)}\varphi^{(y)} + c^{(6)}\varphi^{(z)} + c^{(7)}u^{(u)} + c^{(8)}v^{(u)} \\ & + c^{(9)}w^{(u)} + c^{(10)}u^{(l)} + c^{(11)}v^{(l)} + c^{(12)}w^{(l)} \end{aligned} \tag{8}$$

Here, the coefficients a's, b's, and c's are the function of material properties, thickness coordinates, and the unit step function.

In the present study, nine-noded C-0 isoparametric FE having twelve degrees of freedom per node is used. The associated d.o.f. per node are $\{u^{(0)}, v^{(0)}, w^{(0)}, \varphi^{(x)}, \varphi^{(y)}, \varphi^{(z)}, u^{(u)}, v^{(u)}, w^{(u)}, u^{(l)}, v^{(l)}, w^{(l)}\}$.

The generalized displacement for an element can be written as:

$$\{\delta\} = [N_i]\{\delta_i\} \tag{9}$$

Writing strain-displacement relationship in the linear range, and with the help of Eqs. (1) - (6), the strains can be written in the form of unknowns as:

$$\{\bar{\varepsilon}\} = \{\bar{\varepsilon}\}_{Linear} + \{\bar{\varepsilon}\}_{Non-linear} \tag{10}$$

where,

$$\{\bar{\varepsilon}\}_{Linear} = \left[\frac{\partial U_{(x)}}{\partial x}\ \frac{\partial U_{(y)}}{\partial y}\ \frac{\partial U_{(z)}}{\partial z}\ \frac{\partial U_{(x)}}{\partial x} + \frac{\partial U_{(y)}}{\partial y}\ \frac{\partial U_{(x)}}{\partial z} + \frac{\partial U_{(z)}}{\partial x}\ \frac{\partial U_{(y)}}{\partial z} + \frac{\partial U_{(z)}}{\partial x}\right] \quad \text{or} \quad \{\bar{\varepsilon}\}_{Linear} =$$

$[H]\{\varepsilon\}_{Linear}$

$$\{\bar{\varepsilon}\}_{Non-linear}=\begin{bmatrix}\frac{1}{2}\left(\frac{\partial U_{(z)}}{\partial x}\right)^2+\frac{1}{2}\left(\frac{\partial U_{(x)}}{\partial x}\right)^2+\frac{1}{2}\left(\frac{\partial U_{(y)}}{\partial x}\right)^2\\ \frac{1}{2}\left(\frac{\partial U_{(z)}}{\partial y}\right)^2+\frac{1}{2}\left(\frac{\partial U_{(x)}}{\partial y}\right)^2+\frac{1}{2}\left(\frac{\partial U_{(y)}}{\partial y}\right)^2\\ \left(\frac{\partial U_{(z)}}{\partial x}\right)\left(\frac{\partial U_{(z)}}{\partial y}\right)+\left(\frac{\partial U_{(x)}}{\partial x}\right)\left(\frac{\partial U_{(x)}}{\partial y}\right)+\left(\frac{\partial U_{(y)}}{\partial x}\right)\left(\frac{\partial U_{(y)}}{\partial y}\right)\end{bmatrix} \text{ or}$$

$$\{\bar{\varepsilon}\}_{Non-linear}=\frac{1}{2}\begin{bmatrix}\frac{\partial U_{(z)}}{\partial x} & 0 & \frac{\partial U_{(x)}}{\partial x} & 0 & \frac{\partial U_{(y)}}{\partial x} & 0\\ 0 & \frac{\partial U_{(z)}}{\partial y} & 0 & \frac{\partial U_{(x)}}{\partial y} & 0 & \frac{\partial U_{(y)}}{\partial y}\\ \frac{\partial U_{(z)}}{\partial y} & \frac{\partial U_{(z)}}{\partial x} & \frac{\partial U_{(x)}}{\partial y} & \frac{\partial U_{(x)}}{\partial x} & \frac{\partial U_{(y)}}{\partial y} & \frac{\partial U_{(y)}}{\partial x}\end{bmatrix}\begin{Bmatrix}\frac{\partial U_{(z)}}{\partial x}\\ \frac{\partial U_{(z)}}{\partial y}\\ \frac{\partial U_{(x)}}{\partial x}\\ \frac{\partial U_{(x)}}{\partial y}\\ \frac{\partial U_{(y)}}{\partial x}\\ \frac{\partial U_{(y)}}{\partial y}\end{Bmatrix}=\frac{1}{2}[A_G][\Lambda]$$

$$=\frac{1}{2}[H_G][B]\{\delta\}$$

$\{\varepsilon\}$

$$\{u^{(0)}v^{(0)}\ w^{(0)}\ \varphi^{(x)}\ \varphi^{(y)}\ \varphi^{(z)}\ u^{(u)}v^{(u)}\ w^{(u)}\ u^{(l)}v^{(l)}\ w^{(l)}\ \frac{\partial u^{(0)}}{\partial x}\ \frac{\partial u^{(0)}}{\partial y}\ \frac{\partial v^{(0)}}{\partial x}\ \frac{\partial v^{(0)}}{\partial y}$$

$$=\frac{\partial w^{(0)}}{\partial x}\ \frac{\partial w^{(0)}}{\partial y}\ \frac{\partial \varphi^{(x)}}{\partial x}\ \frac{\partial \varphi^{(x)}}{\partial y}\ \frac{\partial \varphi^{(y)}}{\partial x}\ \frac{\partial \varphi^{(y)}}{\partial y}\ \frac{\partial \varphi^{(z)}}{\partial x}\ \frac{\partial \varphi^{(z)}}{\partial y}\ \frac{\partial u^{(u)}}{\partial x}\ \frac{\partial u^{(u)}}{\partial y}\ \frac{\partial v^{(u)}}{\partial x}\ \frac{\partial v^{(u)}}{\partial y}\ \frac{\partial w^{(u)}}{\partial x}\ \frac{\partial w^{(u)}}{\partial y}$$

$$\frac{\partial u^{(l)}}{\partial x}\ \frac{\partial u^{(l)}}{\partial y}\ \frac{\partial v^{(l)}}{\partial x}\ \frac{\partial v^{(l)}}{\partial y}\ \frac{\partial w^{(l)}}{\partial x}\ \frac{\partial w^{(l)}}{\partial y}\}$$

and the elements contained in $[H], [A_G]$ and $[H_G]$ are a function of unit step function and thickness coordinate and $[B]$ is the strain-displacement relationship in Cartesian coordinates.

With the matrix $[B]$ in the above equation, the geometric stiffness matrix $[K_{ge}]$ can be derived and may be written as

$$[K_{ge}]=\sum_{i=1}^{nu+nl}\iiint [B]^T[S^k]\,[B]\mathrm{dxdydz} \tag{11}$$

where $[S^k]$ is the in-plane stress components of the kth layer can be written as

$$[S^k]=\begin{bmatrix}\sigma_{xx} & \tau_{xy} & 0 & 0 & 0 & 0\\ \tau_{xy} & \sigma_{yy} & 0 & 0 & 0 & 0\\ 0 & 0 & \sigma_{xx} & \tau_{xy} & 0 & 0\\ 0 & 0 & \tau_{xy} & \sigma_{yy} & 0 & 0\\ 0 & 0 & 0 & 0 & \sigma_{xx} & \tau_{xy}\\ 0 & 0 & 0 & 0 & \tau_{xy} & \sigma_{yy}\end{bmatrix}$$

The total potential energy of the plate under hygrothermal and transverse load may be written as:

$$\Pi_e = U_s - U_{ext} \tag{12}$$

where, U_s is the plate's strain energy, and U_{ext} is the energy due to external loading.

$$U_s = \frac{1}{2}\sum_{k=1}^{n} \iiint \{\bar{\varepsilon}\}_{linear}{}^T [\bar{C}]_k \{\bar{\varepsilon}\}_{linear} \mathrm{dxdydz} \tag{13}$$

$$U_{s=} \frac{1}{2} \iint \left[\{\varepsilon\}_{linear}{}^T [D] \{\varepsilon\}_{linear}\right] \mathrm{dxdy} \tag{14}$$

where,

$[D] = \sum_{k=1}^{n} \int [H]^T [\bar{C}]_k [H] \mathrm{dz}.$

$$U_{ext} = \frac{1}{2}\sum_{k=1}^{n} \iiint \{\bar{\varepsilon}\}_{Non-linear}{}^T [S^k]_k \{\bar{\varepsilon}\}_{Non-linear} \mathrm{dxdydz} \tag{15}$$

$$U_{ext} = \frac{1}{2}\sum_{k=1}^{n} \iint \{\varepsilon\}_{Non-linear}{}^T [G]_k \{\varepsilon\}_{Non-linear} \mathrm{dxdy} \tag{16}$$

where, $[G] = \sum_{k=1}^{n} \int [H]^T [S^k]_k [H] \mathrm{dz}$. (Refer to Appendix A for studying the difference in the values of non-dimensional critical buckling load for the plate observed when the non-linearity is the strains is not considered).

Now, calculating the elemental potential energy by combining Eqs. (12) and (14) - (16) as

$$\Pi_e = \tfrac{1}{2} \iint \{\delta\}^T [B]^T [D] [B] \{\delta\} d\mathrm{xdy} - \tfrac{1}{2} \iint \{\delta\}^T [B]^T [G] [B] \{\delta\} d\mathrm{xdy} \text{ or}$$
$$\Pi_e = \frac{1}{2} \{\delta\}^T [K_e] \{\delta\} - \frac{1}{2} L_{cr} \{\delta\}^T \left[K_{ge}\right] \{\delta\} \tag{17}$$

where, $\left[K_{ge}\right] = \iint [B]^T [G] [B] \mathrm{dxdy}$ is the geometric stiffness matrix.

By minimizing the Eq. (17) with respect to $\{\delta\}$, we get

$$[K_e] \{\delta\} = \lambda \left[K_{ge}\right] \{\delta\} \tag{18}$$

where, λ is the buckling load factor.

The skyline storage technique is used to store the global stiffness matrix in a single array, and the simultaneous iteration technique is used for solving the buckling Eq. (18).

For skew plates, the displacement components $\{\delta\}$ along the skew edges (parallel to the y-axis) must be transformed from the global axis to the corresponding local axis, i.e., from the X-Y-Z axis to X'-Y'-Z' axis (Fig. 1). Hence, Eq. (9) must be modified and can be re-written as:
$\{\delta\}^T = [N_T] \{\delta_i\}^T$

The following are the material homogenization rules used during the present study:

Power-law: The variation of volume fraction of ceramic V_c as per Type-A power-law (H-Type-A) is: $V_c(z) = \left(\frac{z-h_0}{h_1-h_0}\right)^n$ for $z \in [h_0, h_1]$, $V_c(z) = 1$ for $z \in [h_1, h_2], V_c(z) = \left(\frac{z-h_3}{h_2-h_3}\right)^n$ for $z \in [h_2, h_3]$. $P(z) = P_m + (P_c - P_m) V_c(z)$, where $P(z)$ is the property of the material at the height z and subscript c, m represents ceramic and metal, respectively (Fig. 2).

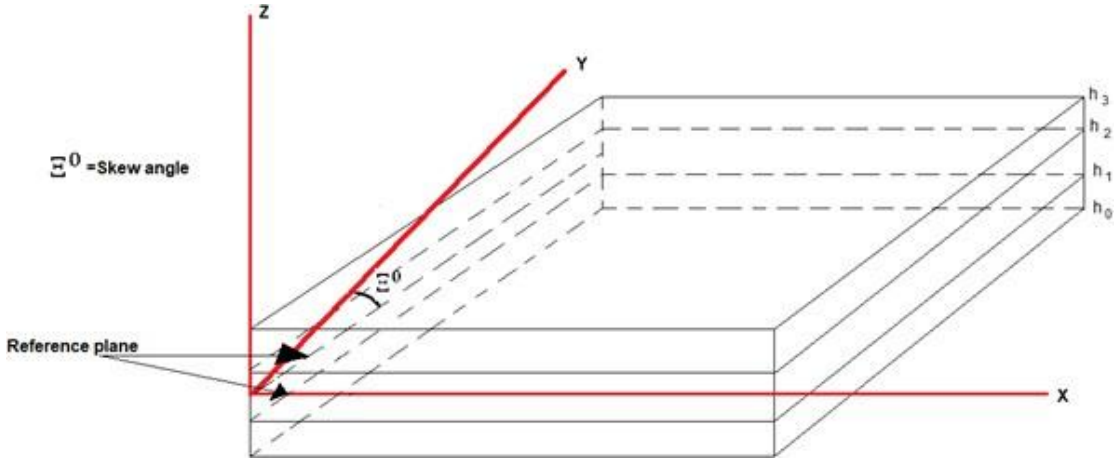

Fig. 1 Geometry of plate

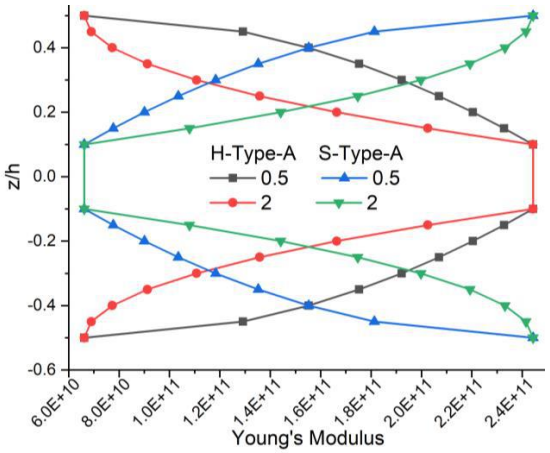

Fig. 2 Young's modulus variation across the thickness of Type-A 2-1-2 sandwich FGM plate

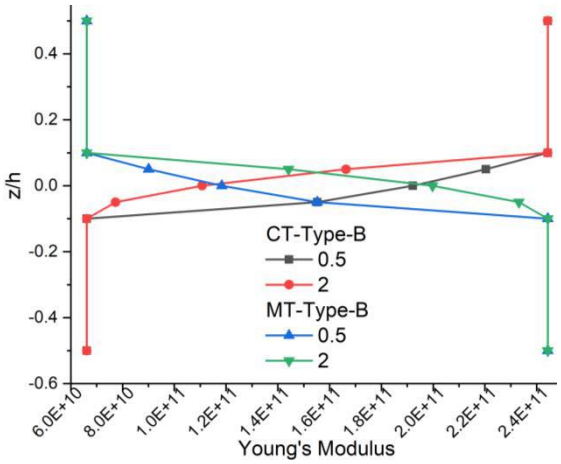

Fig. 3 Young's modulus variation across the thickness of Type-B 2-1-2 sandwich FGM plate

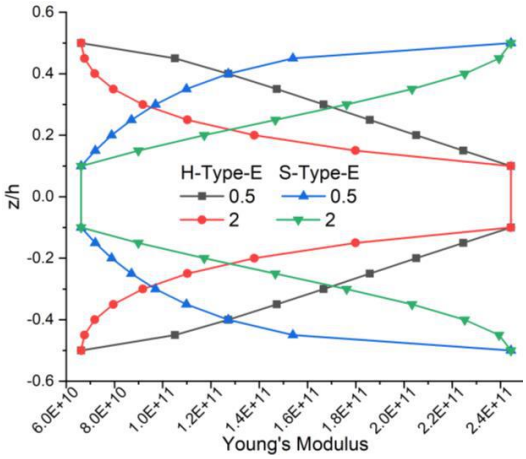

Fig. 4 Young's modulus variation across the thickness of Type-E 2-1-2 sandwich FGM plate

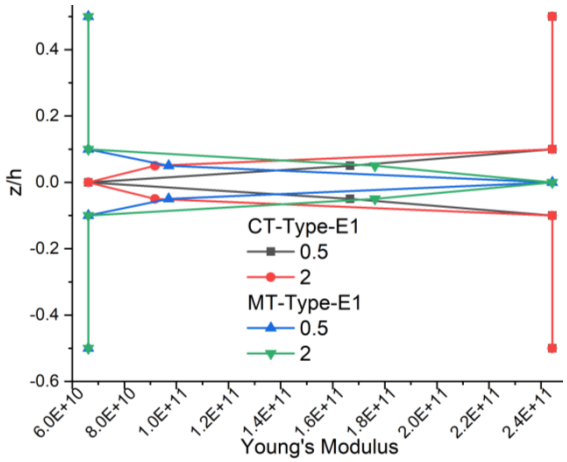

Fig. 5 Young's modulus variation across the thickness of Type-E1 2-1-2 sandwich FGM plate

For Type-B sandwich FGM plate, variation of volume fraction of ceramic across thickness is governed by (CT-Type-B): $V_c(z) = 0$ for $z \in [h_0, h_1]$, $V_c(z) = \left(\frac{z-h_1}{h_2-h_1}\right)^n$ for $z \in [h_1, h_2]$, $V_c(z) = 1$ for $z \in [h_2, h_3]$ (Fig. 3).

Exponential law (Type-E): Governing equations for exponential law (H-Type-E) are as (Fig. 4): $V_c(z) = \left(\frac{2z+1}{2h_1+1}\right)^n$ for $z \in [h_0, h_1]$, $V_c(z) = 1$ for $z \in [h_1, h_2]$, $V_c(z) = \left(\frac{2z-1}{2h_2-1}\right)^n$ for $z \in [h_2, h_3]$. $P(z) = P_m e^{\left(\ln\left(\frac{P_c}{P_m}\right)V_c(z)\right)}$.

Type E1: It is symmetric law in which top and bottom faces are made up of homogenous material and core is made up of FGM (Fig. 5). For Type E1 (CT-Type E1) sandwich FGM beam (Recently proposed by Garg *et al.* 2020b): $V_c(z) = 1$ for $z \in [h_0, h_1]$, $V_c(z) = \left(\frac{z-h_m}{h_1-h_m}\right)^n$ for $z \in [h_1, h_m]$, $V_c(z) = \left(\frac{z-h_m}{h_2-h_m}\right)^n$ for $z \in [h_m, h_2]$, $h_m = (h_1 + h_2)/2$, $V_c(z) = 1$ for $z \in [h_2, h_3]$, $P(z) =$

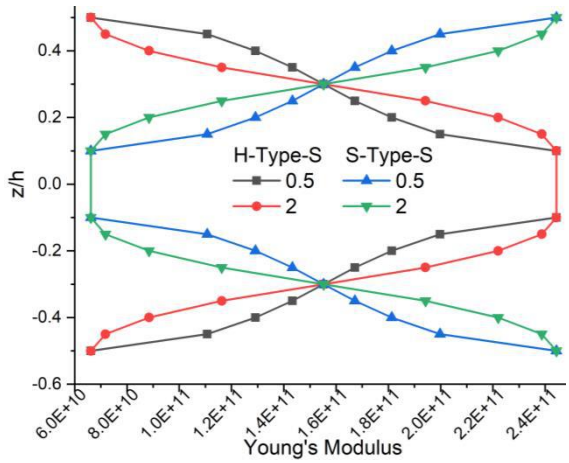

Fig. 6 Young's modulus variation across the thickness of Type-E1 2-1-2 sandwich FGM plate

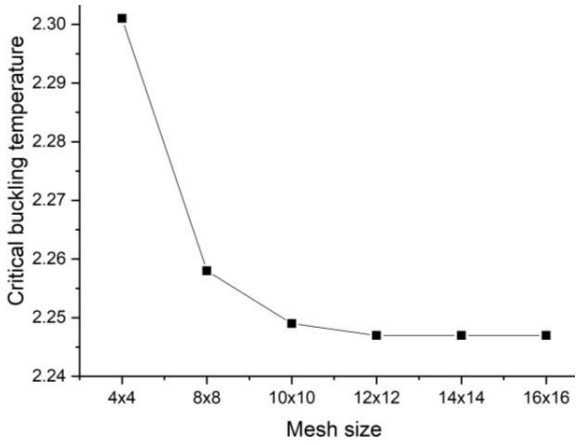

Fig. 7 Convergence study on SSSS 1-1-1 H-Type-A plate

$P_m e^{\left(\ln\left(\frac{P_c}{P_m}\right)V_c(z)\right)}$.

Sigmoidal law: This law is a combination of two power laws: one for a portion of the plate above the central axis and the second one for the portion below the neutral axis. The general sigmoidal law for the sandwich condition is as (Fig. 6): $V_c(z) = 0.5\left(\frac{z-h_0}{h_{m1}-h_0}\right)^n$ for $z \in [h_0, h_{m1}]$ where $h_{m1} = (h_0 + h_1)/2$, $V_c(z) = 1 - 0.5\left(\frac{z-h_1}{h_{m1}-h_1}\right)^n$ for $z \in [h_{m1}, h_1]$, $V_c(z) = 1$ for $z \in [h_1, h_2]V_c$, $V_c(z) = 1 - 0.5\left(\frac{z-h_2}{h_{m2}-h_2}\right)^n$ for $z \in [h_2, h_{m2}]$ where $h_{m2} = (h_2 + h_3)/2$, $V_c(z) = 0.5\left(\frac{z-h_3}{h_{m2}-h_3}\right)^n$ for $z \in [h_{m2}, h_3]$.

3. Results and discussion

In the present study, the metallic phase is assumed to be made up of Titanium ($Ti\ 6Al\ 4V$) and the ceramic phase is assumed to be made up of ($ZrO2$) with material properties as per Table 1

Table 1 Material property

Constituents	Properties			
	$E\ (GPa)$	ν	$\alpha\ (1/°C)$	$\beta\ (wt.\ \%\ H_2O)^{-1}$
Metal $Ti\ 6Al\ 4V$	66.2	0.30	$10.3x10^{-6}$	0.33
Ceramic ZrO_2	244.27	0.30	$12.766x10^{-6}$	0.00

Table 2 Validation study on critical buckling temperature for symmetric H-Type-A sandwich FGM square-shaped plate

a/h	Source	n					
		0.5			2		
		2-1-2	1-1-1	1-2-1	2-1-2	1-1-1	1-2-1
10	Present	0.73773	0.73345	0.74228	0.64543	0.62283	0.63508
	Zenkour and Sobhy2010	0.79220	0.79456	0.80925	0.65075	0.64238	0.66687
5	Present	2.59454	2.57577	2.59825	2.32663	2.24737	2.27892
	Zenkour and Sobhy2010	2.83029	2.83224	2.86971	2.39637	2.35999	2.42873

Zenkour and Sobhy 2010). The plate is made up of three layers and is represented by the thickness of each layer. For example, 2-1-2 represents the thickness of the top face-core-bottom face, respectively (Zenkour 2005a, b).

Convergence study: At first, a convergence study is carried out on the square H-Type-A SSSS sandwich FGM plate (a/h = 5, n = 2, 1-1-1). Results for variation of critical buckling temperature ($T_{cr} = 10^{-3}\Delta T_{cr}$) with different mesh sizes are shown in Fig. 7. Critical buckling temperature ($T_{cr} = 10^{-3}\Delta T_{cr}$) converges at a mesh size of 12x12. Therefore, in further studies, the same mesh size is taken.

Validation study: After establishing the mesh size to be used, a validation study has been carried out in this section. Results of the validation study on the H-Type-A plate under thermal conditions ($T_{cr} = 10^{-3}\Delta T_{cr}$) are reported in Table 2 for different values of a/h (10, 5) and different thickness schemes. The plate is subjected to uniform temperature variation across the thickness of the plate. Present results are compared with those published by Zenkour and Sobhy 2010 using TPT and are found to be in good agreement. It can be observed that as the metallic content increased (increasing the value of n), the value for T_{cr} decreased.

Sandwich FGM plates: In this section, buckling studies are carried out on sandwich FGM plates under hygrothermal conditions. The plate is assumed to be made up of different material laws, thickness schemes, geometric properties etc. The results are reported in the form of tables and figures. Analysis is also carried out on skew sandwich FGM plates.

Power-law sandwich FGM plate: Type-A sandwich FGM plate: Results for critical buckling temperature ($T_{cr} = 10^{-3}\Delta T_{cr}$) for Type-A sandwich FGM plate are reported in Table 3 for four values of a/h (50, 25, 10, 5) and different thickness scheme. The plate is subjected to uniform temperature variation across the thickness of the plate. With an increase in the a/h value, Tcr also increases. The plate with an unsymmetric thickness scheme exhibits more value of T_{cr} for the H-Type-A plate (maximum value of T_{cr} is shown by 2-1-1 followed by 2-2-1 plate when compared between 2-1-2, 2-1-1, 1-1-1, 2-2-1, and 1-2-1). With an increase in the thickness of the core, T_{cr} also increases for both values of n for the H-Type-A plate and n = 2 for the S-Type-A plate. At a lower value of n, the

Table 3 Critical buckling temperature for square-shaped SSSS Type-A sandwich FGM plate

a/h	n	H-Type-A						S-Type-A					
		2-1-2	2-1-1	1-1-1	2-2-1	1-2-1	1-8-1	2-1-2	2-1-1	1-1-1	2-2-1	1-2-1	1-8-1
50	0.5	0.03091	0.03145	0.03074	0.03142	0.03115	0.03493	0.06098	0.06346	0.06294	0.06350	0.06449	0.06214
	2	0.02678	0.02848	0.02583	0.02757	0.02639	0.03217	0.05463	0.05795	0.05859	0.06006	0.06265	0.06527
25	0.5	0.12290	0.12549	0.12222	0.12496	0.12386	0.13877	0.24030	0.25484	0.24789	0.25198	0.25398	0.24544
	2	0.10662	0.11409	0.10285	0.10989	0.10507	0.12789	0.21515	0.23707	0.23007	0.23952	0.24604	0.25723
10	0.5	0.73773	0.76014	0.73345	0.74982	0.74228	0.82759	1.36269	1.52820	1.40064	1.45888	1.43415	1.41173
	2	0.64543	0.70216	0.62283	0.66665	0.63508	0.76611	1.21512	1.48692	1.28467	1.39975	1.36671	1.45866
5	0.5	2.59454	2.71181	2.57577	2.63132	2.59825	2.85774	4.14863	5.20093	4.22826	4.59757	4.32179	4.44001
	2	2.32663	2.59572	2.24737	2.40737	2.27892	2.67860	3.66719	5.08388	3.77973	4.44594	3.97223	4.43606

Table 4 Critical buckling moisture concentration for square-shaped SSSS Type-A sandwich FGM plate

a/h	n	H-Type-A						S-Type-A					
		2-1-2	2-1-1	1-1-1	2-2-1	1-2-1	1-8-1	2-1-2	2-1-1	1-1-1	2-2-1	1-2-1	1-8-1
50	0.5	0.09687	0.12535	0.12270	0.12560	0.17465	0.52651	0.07714	0.07681	0.07576	0.07380	0.07210	0.05235
	2	0.04711	0.06127	0.06325	0.07005	0.09473	0.36310	0.14654	0.13956	0.13155	0.12185	0.11579	0.06910
25	0.5	0.38457	0.49982	0.48690	0.49861	0.69265	2.08474	0.30660	0.30757	0.29875	0.29259	0.28428	0.20697
	2	0.18731	0.24526	0.25137	0.27901	0.37624	1.43872	0.57808	0.56603	0.51799	0.48420	0.45554	0.27268
10	0.5	2.28469	3.01139	2.88486	2.95269	4.08811	12.1810	1.75130	1.83545	1.70046	1.69537	1.61717	1.19675
	2	1.12342	1.50243	1.50434	1.67457	2.24121	8.44378	3.29881	3.48125	2.92183	2.81428	2.55635	1.55857
5	0.5	7.81388	10.5663	9.79575	9.98583	13.7392	38.6133	5.41330	6.07695	5.21157	5.36944	4.94705	3.80669
	2	3.94531	5.47250	5.25103	5.84906	7.72290	24.9291	10.1655	11.8625	8.76308	8.90150	7.56942	4.81389

value of T_{cr} increases first and then decreases with an increase in the thickness of the core. In both types of plates, the minimum value of T_{cr} is shown by the 2-1-2 plate. H-Type-A plate exhibits a maximum value of T_{cr} at 1-8-1 scheme. This is because the ceramic content is maximum for the 1-8-1 scheme among all the thickness schemes for the H-Type-A plate. For the S-Type-A plate, no clear variation is observed for the same as the maximum value of Tcr is found to depend on the thickness scheme, value of n and a/h. In the case of the S-Type-A plate, metallic content is higher as compared to the H-Type-A plate. The value of the thermal expansion coefficient for metal is less than that of ceramic, the S-Type-A plate exhibits more value of Tcr as compared to the H-Type-A plate.

Figs. 8 and 9 show the variation of T_{cr} for rhombic Type-A sandwich FGM plate for different skew angles (Ξ^0) and thickness scheme (a/h = 5). In general, with an increase in skew angle, the value of T_{cr} also increases for the H-Type-A plate. For S-Type-A plate, the variation in the value of T_{cr} with Ξ^0 depends upon the thickness scheme. Fig. 10 shows a variation of T_{cr} for the CCCC rectangular sandwich FGM Type-A plate under thermal conditions for different values of a/b (a/h = 5, n = 0.5). For both H-Type-A and S-Type-A plates, the value of T_{cr} increases with an increase in the value of a/b, the maximum value is observed for the 1-8-1 thickness scheme in both cases.

Table 4 shows the value of critical buckling moisture concentration ($\bar{C}_{cr} = 10\Delta C_{cr}$) for H-Type-

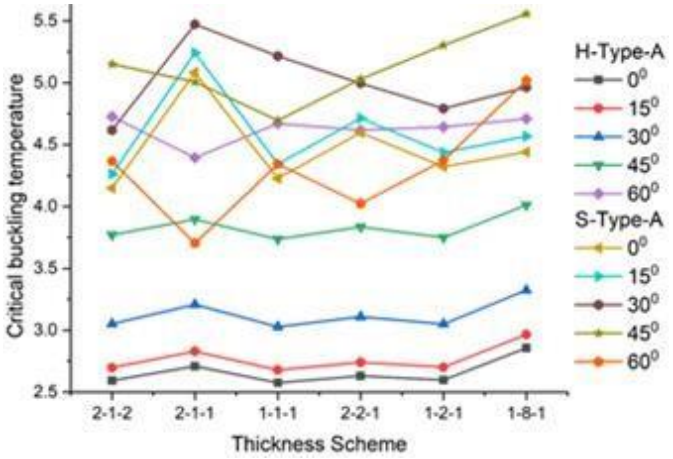

Fig. 8 Variation of critical buckling temperature for SSSS rhombic Type-A sandwich FGM plate (a/h = 5, n = 0.5)

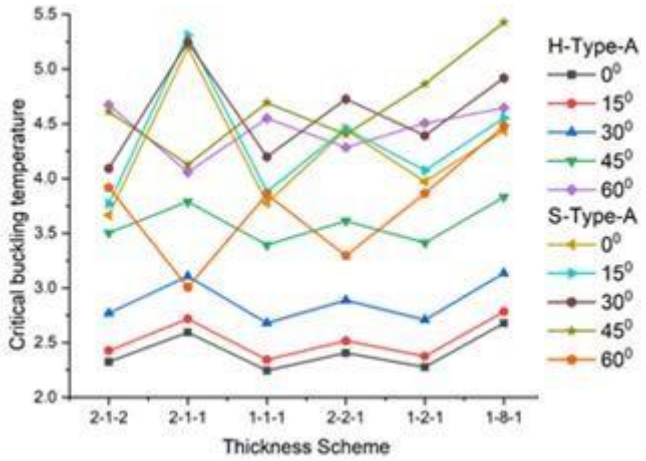

Fig. 9 Variation of critical buckling temperature for SSSS rhombic Type-A sandwich FGM plate (a/h = 5, n = 2)

A and S-type-A sandwich FGM plates with different values of a/h and thickness schemes. With an increase in the value of n, $\bar{C}_{cr}$ decreases for the H-Type-A plate and increases for the S-Type-A plate. The behaviour of H-Type-A and S-Type-A plates in moisture buckling is similar, as seen in the case of thermal buckling. For a lower value of n, H-Type-A gives a higher value of $\bar{C}_{cr}$ and for a higher value of n, S-Type-A decreases for the H-Type-A plate and increases for the S-Type-A plate. The behaviour of H-Type-A and S-Type-A plates in moisture buckling is similar, as seen in the case of thermal buckling. For a lower value of n, H-Type-A gives a higher value of $\bar{C}_{cr}$ and for a higher value of n, the S-Type-A plate gives a higher value of $\bar{C}_{cr}$. For H-Type-A plate, the decrease in buckling moisture load with increasing n could be attributed to the higher concentration of ceramic at the exposed surfaces, which does not expand due to moisture but is brittle. As n increases, making the transition from metal to ceramic steeper, the surface becomes less able to accommodate moisture-induced strains from the metal-rich core, leading to lower buckling loads. With an increase

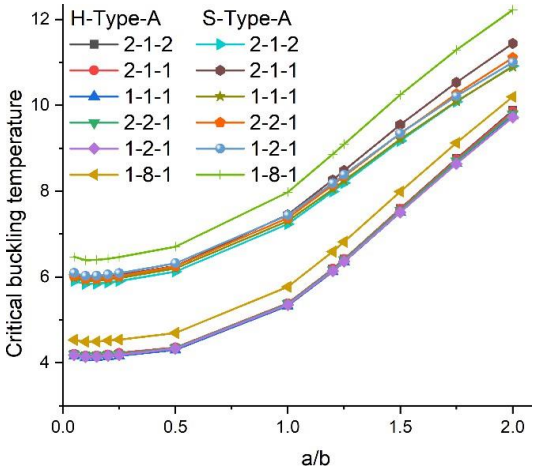

Fig. 10 Variation of critical buckling temperature for CCCC square Type-A sandwich FGM plate (a/h = 5, n = 0.5)

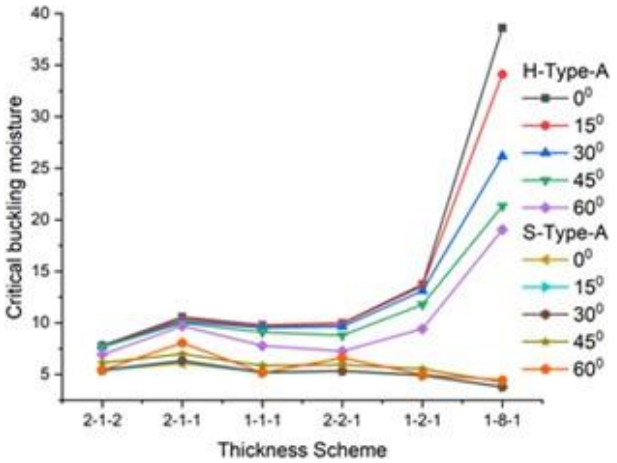

Fig. 11 Variation of critical buckling moisture concentration for SSSS rhombic Type-A sandwich FGM plate (a/h = 5, n = 0.5)

in the ceramic content, the engineering properties of the plate increase which leads to higher stiffness and the plate exhibits a higher value for the buckling load. In the S-Type-A plate, the increase in buckling moisture load with increasing n may be due to the increased presence of metal at the surfaces, which can better tolerate or adapt to moisture-induced expansion. Higher n values mean the metal is more concentrated at the surface, enhancing the overall resilience of the plate to buckling under moisture conditions since the metal can expand without being severely constrained by the non-expanding ceramic. Figs. 11 and 12 show the variation of $\bar{C}_{cr}$ for rhombic sandwich FGM Type-A plate (a/h = 5). The value of $\bar{C}_{cr}$ increases with an increase in the thickness of the core for the H-Type-A plate and decreases for the S-Type-A plate. In general, for the H-Type-A plate, the value of $\bar{C}_{cr}$ decreases with an increase in the value of Ξ^0 while the opposite behaviour is observed for the S-Type-A plate. In general, the plate having higher ceramic content gives a higher value of $\bar{C}_{cr}$ because of the lower value of β as compared to the metallic phase.

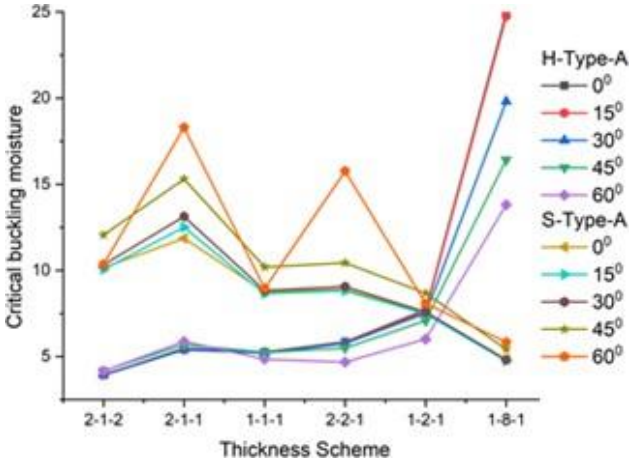

Fig. 12 Variation of critical buckling moisture concentration for SSSS rhombic Type-A sandwich FGM plate (a/h = 5, n = 2)

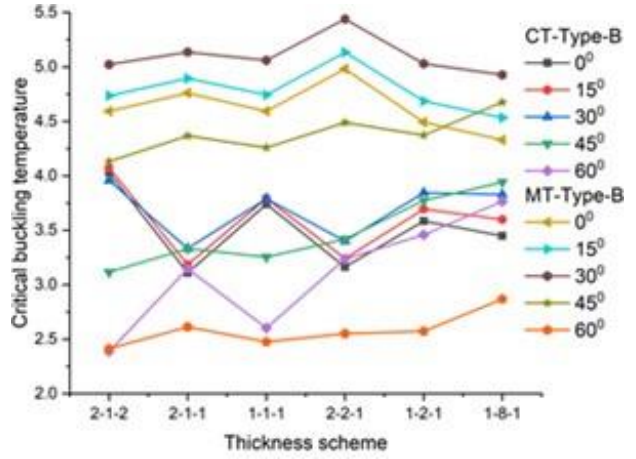

Fig. 13 Variation of critical buckling temperature for SSSS rhombic Type-B sandwich FGM plate (a/h = 5, n = 0.5)

Type-B sandwich FGM plate: Table 5 shows the variation of T_{cr} for SSSS Type-B sandwich FGM plate subjected to the uniform rise of temperature across the plate's thickness. With an increase in the value of n, the value of T_{cr} also increases for the CT-Type-B sandwich FGM beam and decreases for the MT-Type-B sandwich FGM beam. At n = 0.5, the MT-Type-B plate shows a higher value of T_{cr} as compared to the H-Type-B sandwich FGM plate while for n = 2, in some thickness schemes CT-Type-B plate gives a higher value of T_{cr} whereas in other MT- Type-B plate gives higher value. With an increase in core thickness, T_{cr} decreases for the CT-Type-B plate for n = 0.5 whereas increases for n = 2. For the MT-Type-B plate, the opposite trend is observed. Thus, it can be inferred that the value of n and thickness schemes are important factors in determining the sandwich FGM plate's buckling behaviour under thermal conditions.

Figs. 13 and 14 show a variation in critical buckling temperature for SSSS Type-B rhombic plate subjected to constant temperature across the plate thickness for n = 0.5 and 2 (a/h = 5, n = 0.5). For

Table 5 Critical buckling temperature for square-shaped SSSS Type-B sandwich FGM plate

a/h	n	CT-Type-B						MT-Type-B					
		2-1-2	2-1-1	1-1-1	2-2-1	1-2-1	1-8-1	2-1-2	2-1-1	1-1-1	2-2-1	1-2-1	1-8-1
50	0.5	0.04474	0.03727	0.04330	0.03826	0.04318	0.04180	0.05012	0.05960	0.05135	0.05829	0.05108	0.05092
	2	0.05048	0.04052	0.05187	0.04512	0.05529	0.05570	0.04444	0.05486	0.04309	0.04968	0.04085	0.03954
25	0.5	0.17959	0.14819	0.17292	0.15205	0.17178	0.16635	0.20184	0.23734	0.20624	0.23354	0.20482	0.20348
	2	0.20345	0.16170	0.20870	0.18093	0.22214	0.22341	0.17847	0.21994	0.17229	0.20088	0.16268	0.15704
10	0.5	1.10541	0.88824	1.04906	0.90936	1.02917	0.99579	1.25182	1.41096	1.26854	1.41862	1.25294	1.23098
	2	1.26459	0.97951	1.28993	1.10991	1.36636	1.36625	1.10060	1.34034	1.04919	1.24135	0.97813	0.93466
5	0.5	4.02915	3.11032	3.73924	3.16425	3.58560	3.44988	4.59385	4.76032	4.59445	4.98232	4.49350	4.32916
	2	4.65106	3.48791	4.70144	4.02111	4.93279	4.87992	4.02773	4.74079	3.76542	4.56108	3.43119	3.20929

Table 6 Critical buckling moisture for square-shaped SSSS Type-B sandwich FGM plate

a/h	n	CT-Type-B						MT-Type-B					
		2-1-2	2-1-1	1-1-1	2-2-1	1-2-1	1-8-1	2-1-2	2-1-1	1-1-1	2-2-1	1-2-1	1-8-1
50	0.5	0.09348	0.13271	0.09054	0.11664	0.08638	0.10294	0.08366	0.07113	0.07675	0.06611	0.11150	0.12262
	2	0.08450	0.10897	0.07836	0.08623	0.07059	0.07643	0.09573	0.07885	0.09369	0.07838	0.17873	0.36551
25	0.5	0.37635	0.52682	0.36190	0.46313	0.34328	0.40956	0.33790	0.28312	0.30852	0.26455	0.44183	0.48697
	2	0.34178	0.43507	0.31575	0.34622	0.28346	0.30655	0.38584	0.31670	0.37509	0.31625	0.70905	1.45350
10	0.5	2.32909	3.12771	2.19531	2.75261	2.04217	2.44113	2.11144	1.68272	1.90240	1.60375	2.64828	2.90726
	2	2.14343	2.62539	1.95953	2.12784	1.73687	1.86733	2.39860	1.94140	2.28689	1.97173	4.22515	8.72780
5	0.5	8.47553	10.6754	7.77707	9.41799	6.95609	8.32769	7.81184	5.68566	6.90847	5.62723	9.26623	10.0724
	2	7.95983	9.17075	7.17327	7.68976	6.17792	6.54095	8.82545	6.93692	8.17266	7.28240	14.6588	30.6646

both CT-Type-B and MT-Type-B plates, the value of T_{cr} increases with an increase in the value of Ξ^0. At $\Xi^0 = 30^0$, the maximum value of T_{cr} is obtained. After that, the value of T_{cr} starts decreasing with an increase in the value of Ξ^0. Fig. 15 shows the variation of T_{cr} for CCCC rectangular Type-B plate with different values of a/b. In general, with an increase in the value of a/b, T_{cr} also increases.

Table 6 shows the variation of $\bar{C}_{cr}$ for SSSS square-shaped Type-B sandwich FGM plate subjected to constant rise or fall of moisture concentration across the plate's thickness. With an increase in the value of n, the value of $\bar{C}_{cr}$ decreases with an increase in the value of a/h for the CT-Type-B plate. An opposite trend is observed for the same for the MT-Type-B sandwich FGM plate. The maximum value of $\bar{C}_{cr}$ is found to be dependent on the value of n, thickness scheme, and type of plate. Figs. 16 and 17 show the variation of $\bar{C}_{cr}$ for different values of Ξ^0 for Type-B plate (a/h = 5). The value of $\bar{C}_{cr}$ depends widely on Ξ^0 and the thickness scheme of the plate.

Type-E sandwich FGM plate: Table 7 shows the variation of critical buckling temperature for H-type-E and S-Type-E sandwich FGM plates subjected to constant rise/fall of temperature across the plate's thickness. It is observed that with an increase in the value of n, the value of T_{cr} falls for both H-Type-E and S-Type-E plates. 1-8-1 plate shows the maximum value of T_{cr} for the H-Type-E plate and the minimum value for the S-Type-E plate. The value of T_{cr} for the S-Type-E plate is found to be more than the corresponding S-Type-E plate. Among Type-A, B, and E plates, the maximum

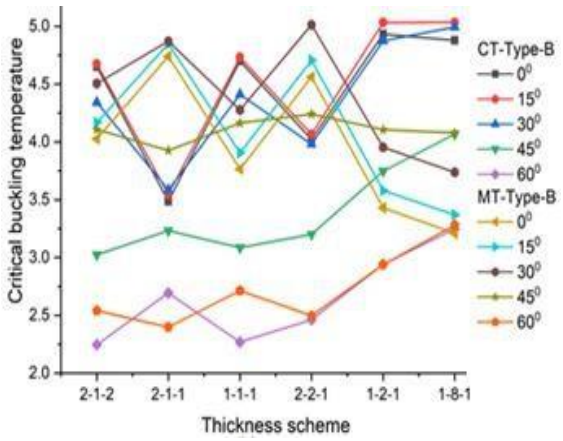

Fig. 14 Variation of critical buckling temperature for SSSS rhombic Type-B sandwich FGM plate (a/h = 5, n = 2)

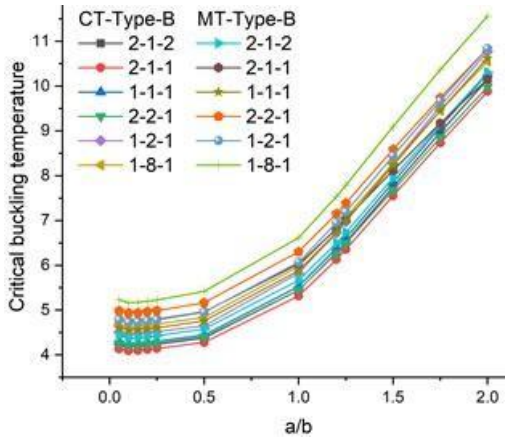

Fig. 15 Variation of critical buckling temperature for CCCC square Type-B sandwich FGM plate (a/h = 5, n = 0.5)

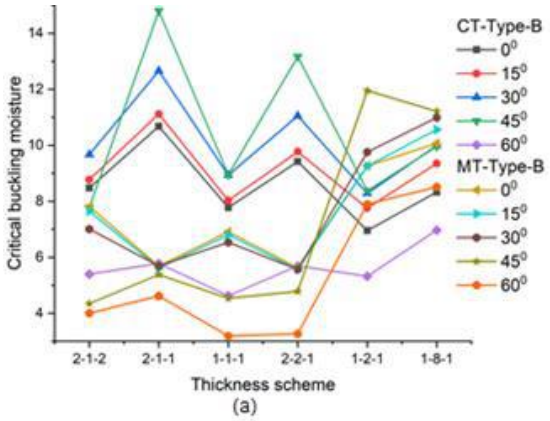

Fig. 16 Variation of critical buckling moisture concentration for SSSS rhombic Type-B sandwich FGM plate (a/h = 5, n = 0.5)

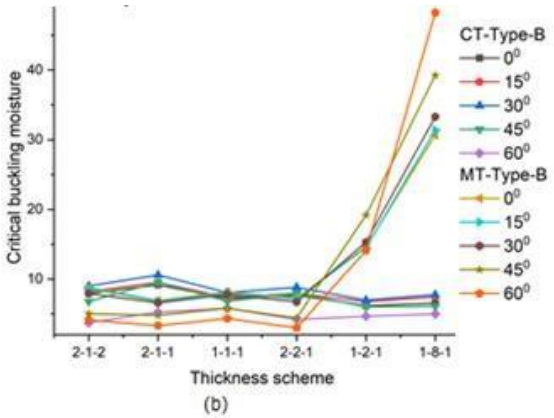

Fig. 17 Variation of critical buckling moisture concentration for SSSS rhombic Type-B sandwich FGM plate (a/h = 5, n = 2)

Table 7 Critical buckling temperature for square-shaped SSSS Type-E sandwich FGM plate

a/h	n	H-Type-E						S-Type-E					
		2-1-2	2-1-1	1-1-1	2-2-1	1-2-1	1-8-1	2-1-2	2-1-1	1-1-1	2-2-1	1-2-1	1-8-1
50	0.5	0.02929	0.03022	0.02905	0.02997	0.02960	0.03408	0.06164	0.06384	0.06291	0.06312	0.06388	0.06045
	2	0.02667	0.02857	0.02508	0.02702	0.02538	0.03153	0.05646	0.05937	0.05984	0.06104	0.06328	0.04636
25	0.5	0.11651	0.12076	0.11558	0.11929	0.11774	0.13541	0.24299	0.25457	0.24792	0.24992	0.25176	0.23895
	2	0.10620	0.11479	0.09988	0.10782	0.10107	0.12538	0.22230	0.24068	0.23525	0.24276	0.24866	0.25379
10	0.5	0.70142	0.73612	0.69554	0.71844	0.70743	0.80860	1.38048	1.49850	1.40622	1.43969	1.42865	1.38027
	2	0.64298	0.71279	0.60553	0.65671	0.61190	0.75187	1.25216	1.47499	1.31438	1.40818	1.38558	1.44433
5	0.5	2.48750	2.66186	2.46387	2.54478	2.49495	2.80217	4.21957	4.85950	4.28168	4.50800	4.35331	4.38673
	2	2.31849	2.67221	2.19245	2.39119	2.20649	2.63657	3.75599	5.01771	3.87104	4.42470	4.05418	4.42953

Table 8 Critical buckling moisture concentration for square-shaped SSSS Type-E sandwich FGM plate

a/h	n	H-Type-E						S-Type-E					
		2-1-2	2-1-1	1-1-1	2-2-1	1-2-1	1-8-1	2-1-2	2-1-1	1-1-1	2-2-1	1-2-1	1-8-1
50	0.5	0.54759	1.51962	0.58781	0.62303	0.65240	1.75615	0.20503	0.20715	0.16983	0.14484	0.12003	0.05922
	2	0.14289	0.26061	0.18205	0.21058	0.26704	1.00345	0.47424	0.35522	0.27451	0.21647	0.17209	0.07485
25	0.5	2.16955	4.08925	2.32886	2.47429	2.58435	6.95013	0.98916	0.82528	0.67091	0.57416	0.47414	0.23440
	2	0.56681	1.05416	0.72235	0.84142	1.05930	3.97408	1.87158	1.43315	1.08188	0.86063	0.67784	0.29564
10	0.5	12.7232	23.6921	13.6555	14.6033	15.1380	40.4782	5.70409	4.84961	3.86087	3.34051	2.72675	1.36506
	2	3.35030	6.62486	4.27652	5.08602	6.26137	23.2498	10.7005	8.62832	6.13363	5.01949	3.82987	1.69899
5	0.5	31.1088	55.2893	30.2499	30.6587	28.5858	52.9165	17.9400	15.4802	12.0847	10.6773	8.52606	4.41506
	2	11.2977	24.8096	14.4895	16.9708	17.6191	31.5973	32.9626	27.6354	18.5248	15.9635	11.4780	5.31149

value of T_{cr} is observed for the MT- Type-B plate for thick plate (a/h = 5). At other values of a/h, the maximum value is observed for the S-Type-E plate. Thus, the plate's behaviour is widely affected by material property variation law and its geometric property.

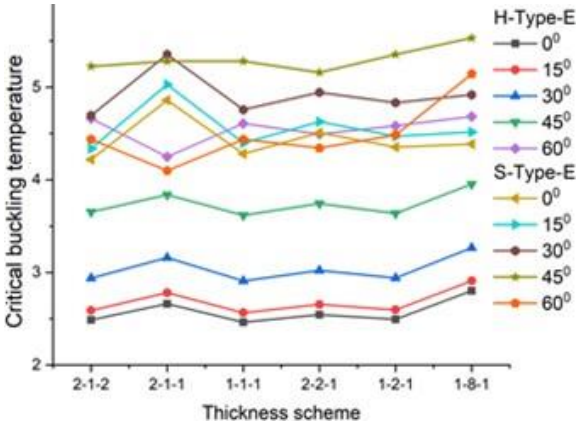

Fig. 18 Variation of critical buckling temperature for SSSS rhombic Type-E sandwich FGM plate (a/h = 5, n = 0.5)

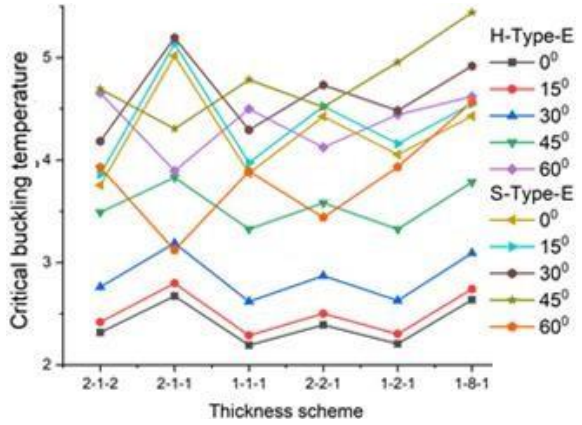

Fig. 19 Variation of critical buckling temperature for SSSS rhombic Type-E sandwich FGM plate (a/h = 5, n = 2)

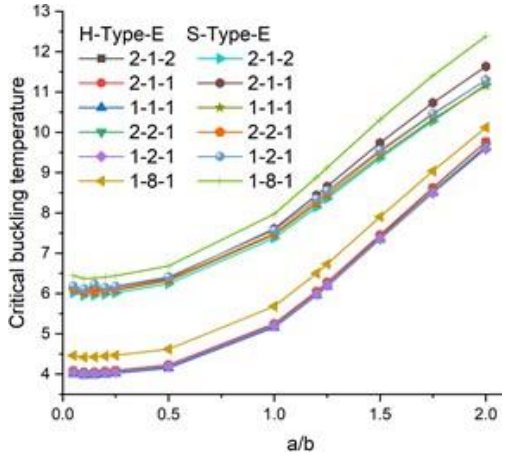

Fig. 20 Variation of critical buckling temperature for CCCC square Type-E sandwich FGM plate (a/h = 5, n = 0.5)

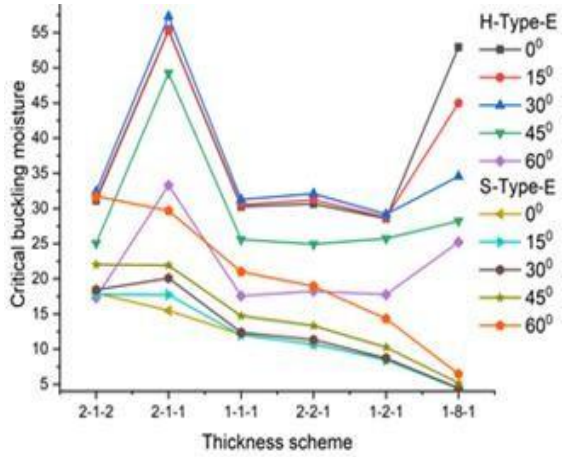

Fig. 21 Variation of critical buckling moisture concentration for SSSS rhombic Type-E sandwich FGM plate (a/h = 5, n = 0.5)

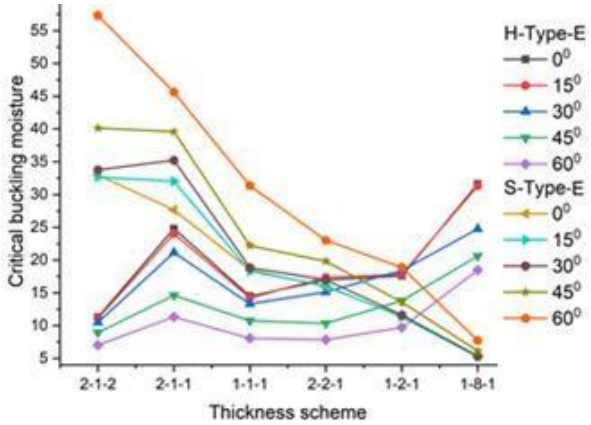

Fig. 22 Variation of critical buckling moisture concentration for SSSS rhombic Type-E sandwich FGM plate (a/h = 5, n = 2)

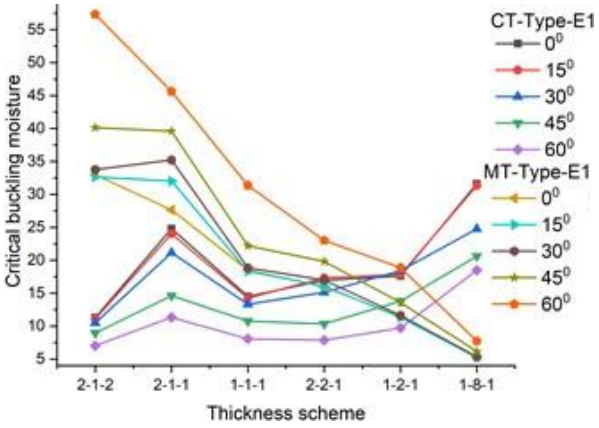

Fig. 23 Variation of critical buckling temperature for SSSS rhombic Type-E1 sandwich FGM plate (a/h = 5, n = 0.5)

Table 9 Critical buckling temperature for square-shaped SSSS Type-E1 sandwich FGM plate

a/h	n	CT-Type-E1						MT-Type-E1					
		2-1-2	2-1-1	1-1-1	2-2-1	1-2-1	1-8-1	2-1-2	2-1-1	1-1-1	2-2-1	1-2-1	1-8-1
50	0.5	0.04441	0.04368	0.04653	0.04719	0.04922	0.05306	0.03489	0.04271	0.03319	0.03832	0.03154	0.03058
	2	0.04599	0.04589	0.04987	0.05217	0.05525	0.06315	0.03168	0.03758	0.02800	0.03094	0.02568	0.02674
25	0.5	0.17566	0.17784	0.18378	0.19256	0.19425	0.20931	0.13864	0.17228	0.13197	0.15477	0.12548	0.12167
	2	0.18152	0.18804	0.19646	0.21190	0.21727	0.24844	0.12596	0.15185	0.11144	0.12471	0.10226	0.10645
10	0.5	1.01519	1.12466	1.05676	1.21759	1.11125	1.19488	0.69498	1.07314	0.79123	0.97030	0.75493	0.73339
	2	1.03986	1.19904	1.11124	1.31026	1.21597	1.39417	0.75552	0.95179	0.67264	0.78018	0.61973	0.64347
5	0.5	2.70996	4.41383	3.32062	4.43065	3.45047	3.69215	0.69733	3.96443	1.55315	3.64151	2.67108	2.60994
	2	3.24077	4.38117	3.36534	4.54025	3.59483	4.14305	1.75747	3.55804	2.40288	2.94774	2.24127	2.30981

Table 10 Critical buckling moisture concentration for square-shaped SSSS Type-E1 sandwich FGM plate

a/h	n	CT-Type-E1						MT-Type-E1					
		2-1-2	2-1-1	1-1-1	2-2-1	1-2-1	1-8-1	2-1-2	2-1-1	1-1-1	2-2-1	1-2-1	1-8-1
50	0.5	1.12488	4.33015	1.11491	2.17854	1.08745	0.99064	0.03824	0.04009	0.04482	0.05217	0.10919	0.24393
	2	1.07670	1.46329	0.80326	0.97498	0.58281	0.38605	0.03878	0.04247	0.04780	0.05787	0.13715	0.42955
25	0.5	4.45631	17.4739	4.41358	8.86266	4.30188	3.91798	0.15161	0.16207	0.17774	0.21143	0.43257	0.96577
	2	4.25954	5.95707	3.17155	3.95357	2.29760	1.52154	0.15386	0.17221	0.18977	0.23413	0.54425	1.70258
10	0.5	26.1042	108.479	25.7326	55.9835	24.9691	22.7052	0.28463	1.01314	0.64530	1.33186	1.65066	5.05940
	2	24.7309	37.5489	18.1874	24.5036	13.0488	8.62174	0.72741	1.08641	1.12701	1.47189	3.22344	10.0106
5	0.5	85.5244	392.914	83.2738	205.770	79.8577	72.2928	0.28531	3.74604	0.64813	4.97972	1.61825	4.98291
	2	79.2044	136.314	56.4866	85.9124	39.5663	25.8367	0.73059	4.07336	3.25611	5.51845	10.8967	29.8502

Figs. 18 and 19 show the variation of T_{cr} for different values of Ξ^0 for the Type-E plate. For the H-Type-E plate, with an increase in the value of Ξ^0, T_{cr} also increases. But for the S-Type-E plate, the value of T_{cr} increases till $\Xi^0 = 45^0$ and then decreases for n = 0.5. For n = 2, the maximum value of T_{cr} is found to be dependent on the thickness scheme for the S-Type-E plate as for symmetric thickness schemes, the maximum value is observed at $\Xi^0 = 45^0$ whereas for unsymmetric schemes, the maximum value is observed at $\Xi^0 = 300$. Fig. 20 shows the variation of Tcr for different values of a/b for CCCC Type-E plate (a/h = 5, n = 0.5). In both types of Type-E plates, the maximum value of Tcr is observed at a 1-8-1 scheme.

Table 8 shows the variation of $\bar{C}_{cr}$ for SSSS Type-E sandwich FGM plate subjected to the equal rise or fall of moisture concentration across the plate's thickness. With an increase in the value of n, the value of $\bar{C}_{cr}$ decreases for the H-Type-E plate and increases for the S-Type-E plate. The plate with the 1-8-1 thickness scheme gives the maximum value of $\bar{C}_{cr}$ for the H-Type-E plate and the minimum value for the S-Type-E plate. Among Type-A, B, and E plates, H-Type-E plates maximum value of $\bar{C}_{cr}$ for n = 0.5 and S-Type-E plate for n = 2. Figs. 21 and 22 shows the variation of $\bar{C}_{cr}$ for different values of Ξ^0. From the figure; it is observed that for the H-Type-E plate, the value of $\bar{C}_{cr}$ decreases with an increase in the value of Ξ^0 whereas for the S-Type-E plate, the opposite behavior is observed.

Type-E1 sandwich FGM plate: Table 9 shows the value of T_{cr} for SSSS Type-E1 sandwich FGM

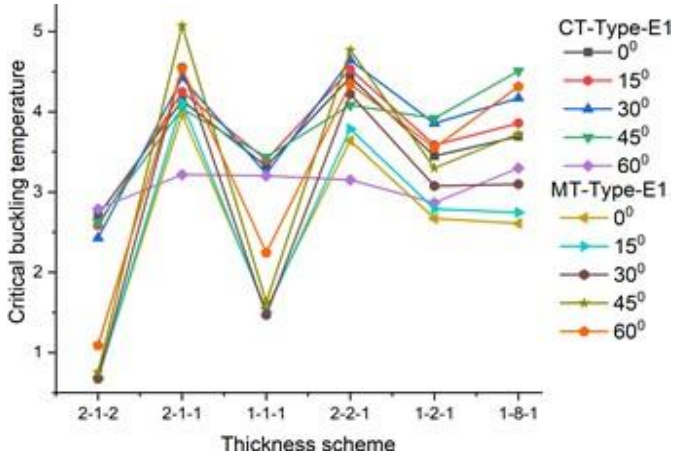

Fig. 24 Variation of critical buckling temperature for SSSS rhombic Type-E1 sandwich FGM plate (a/h = 5, n = 2)

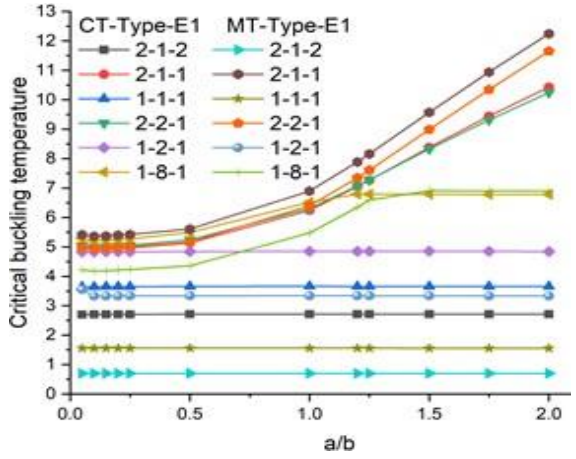

Fig. 25 Variation of critical buckling temperature for CCCC square Type-E1 sandwich FGM plate (a/h = 5, n = 0.5)

Table 11 Critical buckling temperature for square-shaped SSSS Type-S sandwich FGM plate

a/h	n	H-Type-S						S-Type-S					
		2-1-2	2-1-1	1-1-1	2-2-1	1-2-1	1-8-1	2-1-2	2-1-1	1-1-1	2-2-1	1-2-1	1-8-1
50	0.5	0.03072	0.03316	0.02974	0.02102	0.02972	0.03458	0.05649	0.06117	0.05995	0.04248	0.06339	0.06329
	2	0.02650	0.02991	0.02698	0.01931	0.02840	0.03421	0.05983	0.06293	0.06264	0.04316	0.06507	0.06364
25	0.5	0.12222	0.13344	0.11831	0.08226	0.11822	0.13738	0.22276	0.25082	0.23604	0.16348	0.24941	0.24989
	2	0.10551	0.11917	0.10738	0.07512	0.11301	0.13595	0.23527	0.25150	0.24610	0.16080	0.25578	0.25124
10	0.5	0.73456	0.82963	0.71219	0.43640	0.71080	0.81977	1.26860	1.58774	1.33200	0.75505	1.40071	1.43335
	2	0.63810	0.72170	0.64847	0.39360	0.68056	0.81211	1.31707	1.47986	1.37290	0.67098	1.42883	1.43983
5	0.5	2.60513	3.09003	2.52493	1.13445	2.51160	2.83519	3.90119	5.64546	4.01106	1.69881	4.17028	4.47775
	2	2.29362	2.59417	2.32081	1.00553	2.41609	2.81734	3.89597	4.74917	4.02817	1.33131	4.20281	4.48904

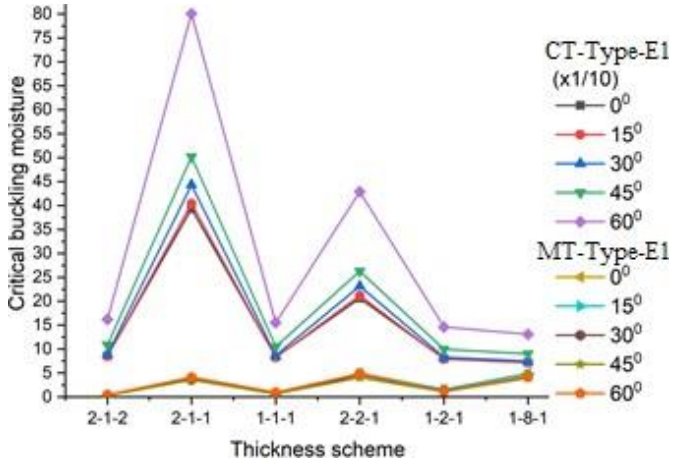

Fig. 26 Variation of critical buckling moisture concentration for SSSS rhombic Type-E1 sandwich FGM plate (a/h = 5, n = 0.5)

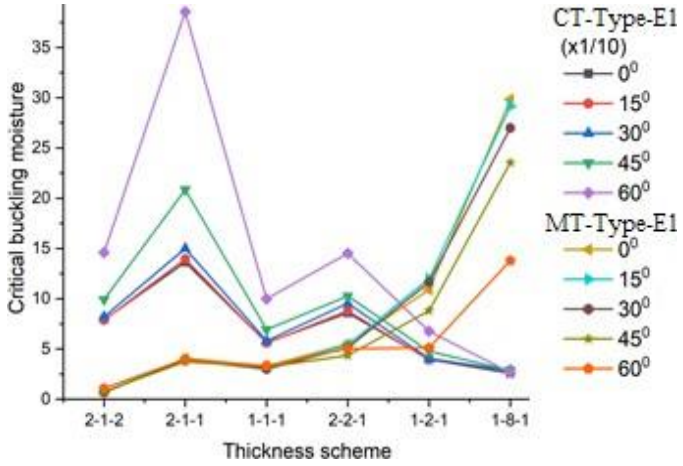

Fig. 27 Variation of critical buckling moisture concentration for SSSS rhombic Type-E1 sandwich FGM plate (a/h = 5, n = 2)

Table 12 Critical buckling moisture concentration for square-shaped SSSS Type-S sandwich FGM plate

a/h	n	H-Type-S						S-Type-S					
		2-1-2	2-1-1	1-1-1	2-2-1	1-2-1	1-8-1	2-1-2	2-1-1	1-1-1	2-2-1	1-2-1	1-8-1
50	0.5	0.06286	0.13104	0.08060	0.08900	0.11696	0.45382	0.09084	0.11895	0.08822	0.06361	0.08326	0.05382
	2	0.06850	0.16787	0.09152	0.10684	0.13699	0.58201	0.11883	0.13641	0.10772	0.07013	0.09348	0.05711
25	0.5	0.24974	0.52448	0.32011	0.34564	0.46421	1.79736	0.35864	0.48427	0.34782	0.24139	0.32801	0.21266
	2	0.27222	0.66625	0.36352	0.41477	0.54367	2.30513	0.46810	0.54351	0.42408	0.25910	0.36809	0.22568
10	0.5	1.49074	3.19797	1.90640	1.79008	2.45281	10.5180	2.05694	3.01648	1.97737	1.07159	1.85632	1.22584
	2	1.62746	3.96203	2.16588	2.15545	3.22290	13.4921	2.64705	3.17930	2.38922	1.05475	2.07566	1.30129
5	0.5	5.16572	11.4365	6.56531	3.66106	9.37032	34.6045	6.42161	10.4952	6.04543	1.67587	5.61142	3.86938
	2	5.66434	13.6128	7.46737	3.36050	10.95977	44.4232	7.98413	10.0744	7.14254	1.85616	6.21495	4.10887

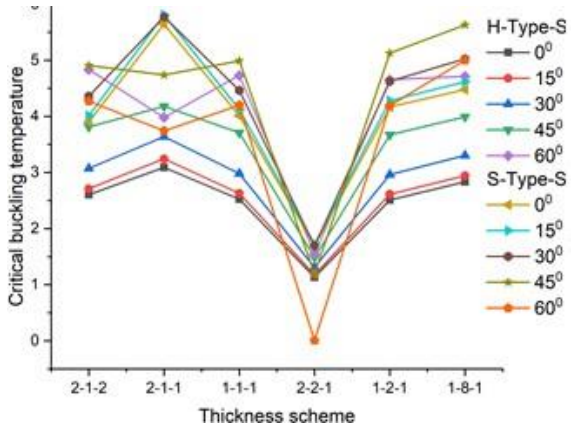

Fig. 28 Variation of critical buckling moisture concentration for SSSS rhombic Type-S sandwich FGM plate for n = 0.5 (a/h = 5)

plate subjected to the equal rise of fall of temperature across the plate's thickness for different thickness schemes and a/h values. It can be seen that very small variation in the value of T_{cr} is observed when the value of n increases from 0.5 to 2 for all cases except for the thick plate (a/h = 5). Even a similar type of trend is observed for variations of $\bar{C}_{cr}$ (Table 10). CT-Type- E1 and S-Type-E plate shows the maximum value of $\bar{C}_{cr}$ and T_{cr} respectively among Type-A, B, E & E1 plates.

Figs. 23 and 24 show the variation of T_{cr} for the SSSS rhombic plate (a/h = 5) for different values of skew angle and thickness schemes. For n = 0.5, with an increase in the value of Ξ^0, the value of T_{cr} decreases for the CT-Type-E1 plate and increases for the MT-Type-E1 plate. But for n = 2, Tcr increases up to $\Xi^0 = 45^0$ and then decreases for the CT-Type-E1 plate. For the MT-Type-E1 plate, T_{cr} increases with an increase in the value of Ξ0. Fig. 25 shows the variation of T_{cr} for the CCCC rectangular CCCC plate (a/h = 5, n =0 .5) for different values of a/b. An interesting behaviour is observed that except for the unsymmetric thickness scheme, the value of T_{cr} remains almost the same for different values of a/b for both CT- & MT-Type-E1 plates. Fig. 26 and 27 show the variation of $\bar{C}_{cr}$ for SSSS rhombic plate (a/h = 5) for different values of skew angle and thickness schemes. The values of $\bar{C}_{cr}$ are scaled down by a tenth. It is seen that for the MT-Type-E1 plate, the value of $\bar{C}_{cr}$ decreases with an increase in the value of Ξ^0. The opposite behaviour is observed for the CT-Type-E1 plate.

Type-S sandwich FGM plate: Table 11 shows the variation of T_{cr} for SSSS Type-S sandwich FGM plate under thermal conditions. With an increase in the value of n, the value of T_{cr} decreases for H-Type-S and increases for the S-Type-S sandwich FGM plate. Only a small change in the value of T_{cr} is observed when the value of n is increased from 0.5 to 2. For both H- and S-Type-S plates, the maximum value of T_{cr} is observed for the 1-8-1 scheme. Table 12 shows the variation of $\bar{C}_{cr}$ for the same plate under hygro conditions. It is seen that the value of $\bar{C}_{cr}$ increases with an increase in the value of n for both types of plates. With an increase in the thickness of the core, the value of $\bar{C}_{cr}$ increases for the H-Type-S plate and decreases for the S-Type-S plate.

Figs. 28 and 29 show the variation of Tcr for the SSSS Type-S rhombic sandwich FGM plate under thermal conditions. For the H-Type-S plate, the value of T_{cr} increases with an increase in the value of Ξ^0 but for S-Type-S, the same increases up to 45° and then decreases. Fig. 30 shows the

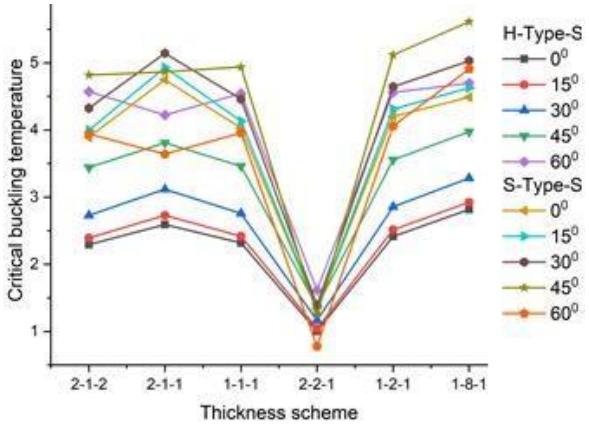

Fig. 29 Variation of critical buckling temperature for SSSS rhombic Type-S sandwich FGM plate for n = 2 (a/h = 5)

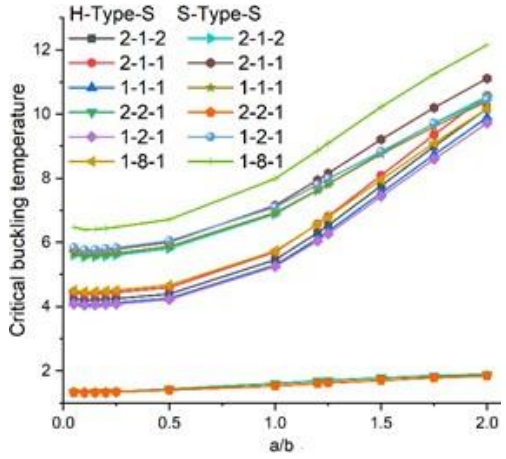

Fig. 30 Variation of critical buckling temperature for CCCC square Type-S sandwich FGM plate (a/h = 5, n = 0.5)

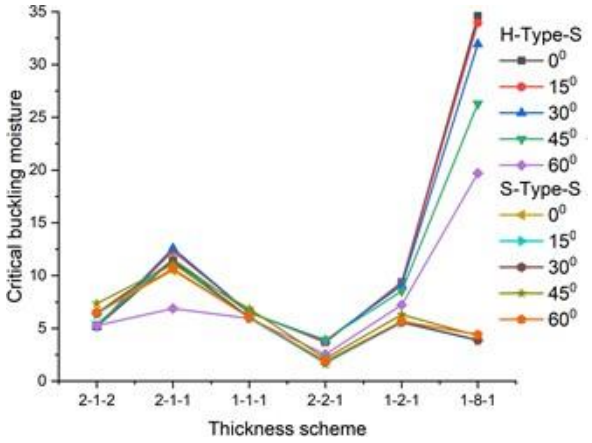

Fig. 31 Variation of critical buckling moisture concentration for SSSS rhombic Type-S sandwich FGM plate for n = 0.5 (a/h = 5)

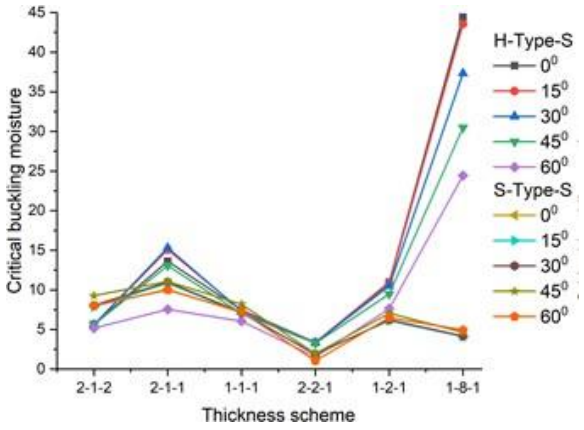

Fig. 32 Variation of critical buckling moisture concentration for SSSS rhombic Type-S sandwich FGM plate for n = 2 (a/h = 5)

variation of T_{cr} for CCCC rectangular Type-S sandwich FGM plate with different values of a/b under thermal loading. For both H-Type-S and S-Type-S plates, the value of T_{cr} increases with an increase in the value of a/b. Figs. 31 and 32 shows the variation of $\bar{C}_{cr}$ for SSSS Type-S rhombic sandwich FGM plate under hygro conditions. For the H-Type-S plate, the value of $\bar{C}_{cr}$ increases with an increase in the value of Ξ^0 but for S-Type-S, the same increases up to 45° and then decreases.

In general, it can be stated that with an increase in ceramic content in the plate, the value for non-dimensional buckling temperature and moisture concentration increases. Hence, the plates having central core made up of ceramic gives higher value for buckling load as compared to the plate in which central core is made up of metal. This is because the value for α and β are less for ceramic as compared to that of metal. Thus, the plate having an overall lesser content of metallic phase gives a higher value of buckling loads.

4. Conclusions

A comparative buckling study has been carried out among power, exponential, and sigmoidal sandwich FGM plates subjected to hygro-thermal conditions in the present work. The study has been carried out using FE-based HOZT considering transverse displacement effects/transverse strain effects. The present formulation is free from the requirement of any penalty function or post-processing technique and hence is computationally efficient. The following important points are noted down:

• The choice of material homogenization rule widely affects the buckling behaviour of sandwich FGM plates under hygro-thermal conditions.

• Because of very little thickness in very thin sandwich FGM plates (a/h = 50), only minor change is observed in critical buckling temperature and moisture concentration.

• The CT-Type-E1 plate shows the maximum value of critical buckling moisture because of the large proportion of ceramic compared to the metallic phase.

• S-Type-E plate shows the maximum value of critical buckling temperature among all the material variation laws studied.

• The degree of skewness also affects the buckling behaviour of sandwich FGM plates to a great extent.

• The behaviour of skew sandwich FGM plates with unsymmetric thickness schemes is different from skew plates with symmetric configurations.

• In symmetric FGM sandwich structures, the material properties are distributed symmetrically about the mid-plane. This means the top and bottom layers have identical gradients, typically with a core material that is different but centrally aligned. The symmetry ensures that the thermal expansion is balanced, reducing bending effects due to uniform expansion.

• Ceramic-dominated plates (plates with more ceramic content compared to metallic content) show a large value of critical buckling moisture and temperature.

• Such a comparative study has been carried out and will serve as a benchmark for future results as new results are presented in present work for exponential, sigmoidal, and power-law plates.

Acknowledgment

This work is partially supported by the Innovation-Driven Development Special Fund Project of Guangxi (Grant No. Guike AA23062040), the Key Research and Development Program of Guangxi (Grant No. Guike AB23026106), the National Natural Science Foundation of China (Grant No. 52175095), the Science and Technology Planning Project of Liuzhou (Grant Nos. 2022AAA0102, and 2022AAA0104), and the Young Top-notch Talent Cultivation Program of Hubei Province of China.

References

Adhikari, B., Dash, P. and Singh, B.N. (2020), "Buckling analysis of porous FGM sandwich plates under various types nonuniform edge compression based on higher order shear deformation theory", *Compos. Struct.*, **251**, 112597. https://doi.org/10.1016/j.compstruct.2020.112597.

Akavci, S.S. (2016), "Mechanical behavior of functionally graded sandwich plates on elastic foundation", *Compos. Part B Eng.*, **96**, 136-152. https://doi.org/10.1016/j.compositesb.2016.04.035.

Al-Osta, M.A., Saidi, H., Tounsi, A., Al-Dulaijan, S.U., Al- Zahrani, M.M., Sharif, A. and Tounsi, A. (2021), "Influence of porosity on the hygro-thermo-mechanical bending response of an AFG ceramic-metal plates using an integral plate model", *Smart Struct. Syst.*, **28**(4), 499-513. https://doi.org/10.12989/sss.2021.28.4.499.

Al-Osta, M.A. (2022a), "An exponential-trigonometric quasi-3D HSDT for wave propagation in an exponentially graded plate with microstructural defects", *Compos. Struct.*, **297**, 115984. https://doi.org/10.1016/j.compstruct.2022.115984.

Al-Osta, M.A. (2022b), "Wave propagation investigation of a porous sandwich FG plate under hygrothermal environments via a new first-order shear deformation theory", *Steel Compos. Struct.*, **43**(1), 117-127. https://doi.org/10.12989/scs.2022.43.1.117.

Alnujaie, A., Akbaş, S.D., Eltaher, M.A. and Assie, A.E. (2021), "Damped forced vibration analysis of layered functionally graded thick beams with porosity", *Smart Struct. Syst.*, **27**(4), 669-689. https://doi.org/10.12989/sss.2021.27.4.669.

Barati, M.R. and Zenkour, A.M. (2019a), "Analysis of postbuckling behavior of general higher-order functionally graded nanoplates with geometrical imperfection considering porosity distributions", *Mech. Adv. Mater. Struct.*, **26**(12), 1081- 1088. https://doi.org/10.1080/15376494.2018.1430280.

Barati, M.R. and Zenkour, A.M. (2019b), "Analysis of postbuckling of graded porous GPL-reinforced beams

with geometrical imperfection", *Mech. Adv. Mater. Struct.*, **26**(6), 503-511. https://doi.org/10.1080/15376494.2017.1400622.

Belarbi, M.O., Salami, S.J., Garg, A., Hirane, H., Daikh, A.A. and Houari, M.S.A. (2022), "Finite element bending and buckling analysis of functionally graded carbon nanotubes-reinforced composite beam under arbitrary boundary conditions", *Steel Compos. Struct.*, **44**(4), 451-471. https://doi.org/10.12989/scs.2022.44.4.451.

Belarouci, A. and Fekrar, A. (2021), "A new quasi-3D theory for the study of the bending of thick FGM's plates on elastic foundation", *Smart Struct. Syst.*, **27**(5), 847-860. https://doi.org/10.12989/sss.2021.27.5.847.

Belkhodja, Y., Ouinas, D., Fekirini, H., Viña Olay, J.A., Achour, B., Touahmia, M. and Boukendakdji, M. (2022), "A new hybrid HSDT for bending, free vibration, and buckling analysis of FGM plates (2D & quasi-3D)", *Smart Struct. Syst.*, **29**(3), 395- 420. https://doi.org/10.12989/sss.2022.29.3.395.

Bellifa, H., Selim, M.M., Chikh, A., Bousahla, A.A., Bourada, F., Tounsi, A., Benrahou, K.H., Al-Zahrani, M.M. and Tounsi, A., "Influence of porosity on thermal buckling behavior of functionally graded beams", *Smart Struct. Syst.*, **27**(4), 719-728. https://doi.org/10.12989/sss.2021.27.4.719.

Bouazza, M. and Zenkour, A.M. (2020), "Hygro-thermo- mechanical buckling of laminated beam using hyperbolic refined shear deformation theory", *Compos. Struct.*, **252**, 112689. https://doi.org/10.1016/j.compstruct.2020.112689.

Brischetto, S. (2009), "Classical and mixed advanced models for sandwich plates embedding functionally graded cores", *J. Mech. Mater. Struct.*, **4**, 13-33. https://doi.org/10.2140/jomms.2009.4.13.

Carrera, E., Brischetto, S., Cinefra, M. and Soave, M. (2011), "Effects of thickness stretching in functionally graded plates and shells", *Compos. Part B Eng.*, **42**, 123-133. https://doi.org/10.1016/j.compositesb.2010.10.005.

Civalek, O., Uzun, B. and Yayli, M.O. (2022), "A Fourier sine series solution of static and dynamic response of nano/micro-scaled FG rod under torsional effect", *Adv, Nano Res.*, **12**(5), 467-482. https://doi.org/10.12989/anr.2022.12.5.467.

Cuong-Le, T., Nguyen, K.D., Hoang-Le, M., Sang-To, T., Phan-Vu, P. and Wahab, M.A. (2022a), "Nonlocal strain gradient IGA numerical solution for static bending, free vibration and buckling of sigmoid FG sandwich nanoplate", *Physica B Condens.*, **631**, 413726. https://doi.org/10.1016/j.physb.2022.413726.

Cuong-Le, T., Hoang-Le, M., Ferreira, A.J.M. and Wahab M.A. (2022b), "Small size-effect isogeometric analysis for linear and nonlinear responses of porous metal foam microplate", *Compos. Struct.*, **285**, 115189. https://doi.org/10.1016/j.compstruct.2022.115189.

Cuong-Le, T., Nguyen, T.N., Vu, T.H., Khatir, S. and Wahab, M.A. (2022c), "A geometrically nonlinear size-dependent hypothesis for porous functionally graded micro-plate", *Eng. Comput.*, **38**, 449-460. https://doi.org/10.1007/s00366-020-01154-0.

Daikh, A.A. and Zenkour, A.M. (2019), "Free vibration and buckling of porous power-law and sigmoid functionally graded sandwich plates using a simple higher-order shear deformation theory", *Mater. Res. Express.*, **6**(11), 115707. https://doi.org/10.1088/2053-1591/ab48a9.

Di Sciuva, M. and Sorrenti, M. (2021), "Bending and free vibration analysis of functionally graded sandwich plates: An assessment of the Refined Zigzag Theory", *J. Sandw. Struct. Mater.*, **23**(3), 760-802. https://doi.org/10.1177/1099636219843970.

Dorduncu, M. (2020), "Stress analysis of sandwich plates with functionally graded cores using peridynamic differential operator and refined zigzag theory", *Thin-Walled Struct.*, **146**, 106468. https://doi.org/10.1016/j.tws.2019.106468.

Fazzolari, F.A. (2018), "Generalized exponential, polynomial and trigonometric theories for vibration and stability analysis of porous FG sandwich beams resting on elastic foundations", *Compos. Part B Eng.*, **136**, 254-271. https://doi.org/10.1016/j.compositesb.2017.10.022.

Fazzolari, F.A. (2016), "Stability analysis of FGM sandwich plates by using variable-kinematics Ritz models", *Mech. Adv. Mater. Struct.*, **23**(9), 1104-1113. https://doi.org/10.1080/15376494.2015.1121559.

Fazzolari, F.A. and Carrera, E. (2014), "Thermal stability of FGM sandwich plates under various through-the-thickness temperature distributions", *J. Therm. Stress.*, **37**(12), 1449- 1481.

https://doi.org/10.1080/01495739.2014.937251.
Garg, A. and Chalak, H.D. (2019), "A review on analysis of laminated composite and sandwich structures under hygrothermal conditions", *Thin-Walled Struct.*, **142**, 205-226. https://doi.org/10.1016/j.tws.2019.05.005.
Garg, A., Chalak, H.D. and Chakrabarti, A. (2020a), "Bending analysis of functionally graded sandwich plates using HOZT including transverse displacement effects", *Mech. Based Des. Struct.*, **50**(10), 1-15. https://doi.org/10.1080/15397734.2020.1814157.
Garg, A., Chalak, H.D. and Chakrabarti, A. (2020b), "Comparative study on the bending of sandwich FGM beams made up of different material variation laws using refined layerwise theory", *Mech. Mater.*, **151**, 103634. https://doi.org/10.1016/j.mechmat.2020.103634.
Garg, A. and Chalak, H.D. (2021), "Analysis of non-skew and skew laminated composite and sandwich plates under hygro- thermo-mechanical conditions including transverse stress variations", *J. Sandw. Struct. Mater.*, **23**(8), 3471-3494. https://doi.org/10.1177/1099636220932782.
Garg, A., Belarbi, M.O., Chalak, H.D. and Chakrabarti, A. (2021a), "A review of the analysis of sandwich FGM structures", *Compos. Struct.*, **258**, 113427. https://doi.org/10.1016/j.compstruct.2020.113427.
Garg, A., Chalak, H.D., Belarbi, M.O., Chakrabarti, A. and Houari, M.S.A. (2021b), "Finite element-based free vibration analysis of power-law, exponential and sigmoidal functionally graded sandwich beams", *J. Inst. Eng. C*, **102**(5), 1167-1201. https://doi.org/10.1007/s40032-021-00740-5.
Garg, A., Chalak, H.D., Belarbi, M.O. and Zenkour, A.M. (2021c), "Hygro-thermo-mechanical based bending analysis of symmetric and unsymmetric power-law, exponential and sigmoidal FG sandwich beams", *Mech. Adv. Mater. Struct.*, **29**(25), 4523-4545. https://doi.org/10.1080/15376494.2021.1931993.
Garg, A., Mukhopadhyay, T., Chalak, H.D., Belarbi, M.O., Li, L. and Sahoo R. (2022a), "Multiscale bending and free vibration analyses of functionally graded graphene platelet/ fiber composite beams", *Steel Compos. Struct.*, **44**(5), 707-720. https://doi.org/10.12989/scs.2022.44.5.707.
Garg, A., Belarbi, M.O. Li, L and Tounsi, A. (2022), "Bending analysis of power-law sandwich FGM beams under thermal conditions", *Adv. Aircr. Spacecr. Sci.*, **9**(3), 243-261. https://doi.org/10.12989/aas.2022.9.3.243.
Hadji, L. and Tounsi, A. (2021), "Static deflections and stress distribution of functionally graded sandwich plates with porosity", *Smart Struct. Syst.*, **28**(3), 343-354. https://doi.org/10.12989/sss.2021.28.3.343.
Hosseini, S.A.H., Rahmani, O. and Bayat, S. (2022), "A new solution for dynamic response of FG nonlocal beam under moving harmonic load", *Steel Compos. Struct.*, **43**(2), 185-200. https://doi.org/10.12989/scs.2022.43.2.185.
Iurlaro, L., Gherlone, M. and Di Sciuva, M. (2014), "Bending and free vibration analysis of functionally graded sandwich plates using the Refined Zigzag Theory", *J. Sandw. Struct. Mater.*, **16**(6), 669-699. https://doi.org/10.1177/1099636214548618.
Jalali, S.K., Naei, M.H. and Poorsolhjouy, A. (2010), "Thermal stability analysis of circular functionally graded sandwich plates of variable thickness using pseudo-spectral method", *Mater. Des.*, **31**, 4755-4763. https://doi.org/10.1016/j.matdes.2010.05.009.
Kiani, Y. and Eslami, M.R. (2012), "Thermal buckling and post- buckling response of imperfect temperature-dependent sandwich FGM plates resting on elastic foundation", *Arch. Appl. Mech.*, **82**, 891-905. https://doi.org/10.1007/s00419-011-0599-8.
Kırlangıç, O. and Akbaş, Ş.D. (2021), "Dynamic responses of functionally graded and layered composite beams", *Smart Struct. Syst.*, **27**(1), 115-122. https://doi.org/10.12989/sss.2021.27.1.115.
Kumar, H.S.N. and Kattimani, S. (2022), "Nonlinear analysis of two-directional functionally graded doubly curved panels with porosities", *Struct. Eng. Mech.*, **82**(4), 477-490. https://doi.org/10.12989/sem.2022.82.4.477.
Kurpa, L. V. and Shmatko, T.V. (2020), "Buckling and free vibration analysis of functionally graded sandwich plates and shallow shells by the Ritz method and the R-functions theory", *Proceedings of the Institution of Mechanical Engineers, Part C: Journal of Mechanical Engineering Science*, **235**(20), 4582-4593. https://doi.org/10.1177/0954406220936304.
Lim, T.K. and Kim, J.H. (2017), "Thermo-elastic effects on shear correction factors for functionally graded

beam", *Compos. Part B Eng.*, **123**, 262-270. https://doi.org/10.1016/j.compositesb.2017.05.031.
Love, A.E.H. (1888), "The small free vibrations and deformation of a thin elastic shell", *Philos. Trans. R. Soc. A Math. Phys. Eng. Sci.*, **179**, 491-546. https://doi.org/10.1098/rsta.1888.0016.
Mahi, A., Adda Bedia, E.A. and Tounsi, A. (2015), "A new hyperbolic shear deformation theory for bending and free vibration analysis of isotropic, functionally graded, sandwich and laminated composite plates", *Appl. Math. Model.*, **39**, 2489-2508. https://doi.org/10.1016/j.apm.2014.10.045.
Mashat, D.S. and Zenkour, A.M. (2020), "Modified DPL Green- Naghdi theory for thermoelastic vibration of temperature- dependent nanobeams", *Results Phys.*, **16**, 102845. https://doi.org/10.1016/j.rinp.2019.102845.
Meksi, R., Benyoucef, S., Mahmoudi, A., Tounsi, A., Adda Bedia, E.A. and Mahmoud, S.R. (2019), "An analytical solution for bending, buckling and vibration responses of FGM sandwich plates", *J. Sandw. Struct. Mater.*, **21**(2), 727-757. https://doi.org/10.1177/1099636217698443.
Natarajan, S. and Manickam, G. (2012), "Bending and vibration of functionally graded material sandwich plates using an accurate theory", *Finite Elem. Anal. Des.*, **57**, 32-42. https://doi.org/10.1016/j.finel.2012.03.006.
Neves, A.M.A., Ferreira, A.J.M., Carrera, E., Cinefra, M., Jorge, R.M.N., Soares, C.M.M. and Araújo, A.L. (2017), "Influence of zig-zag and warping effects on buckling of functionally graded sandwich plates according to sinusoidal shear deformation theories", *Mech. Adv. Mater. Struct.*, **24**(5), 360-376. https://doi.org/10.1080/15376494.2016.1191095.
Nguyen, K.D., Cuong-Le T., Nguyen-Xuan, H. and Abdel-Wahab, M. (2021), "A hybrid phase-field isogeometric analysis to crack propagation in porous functionally graded structures", *Eng. Comput.*, 1-21. https://doi.org/10.1007/s00366-021-01518-0.
Nguyen, V.X., Lieu, Q.X., Le, T.A., Nguyen, T.D., Suzuki. T. and Luong, V.H. (2022), "A novel coupled finite element method for hydroelastic analysis of FG-CNTRC floating plates under moving loads", *Steel Compos. Struct.*, **42**(2), 243-256. https://doi.org/10.12989/scs.2022.42.2.243.
Osofero, A.I., Vo, T.P., Nguyen, T.K. and Lee, J. (2016), "Analytical solution for vibration and buckling of functionally graded sandwich beams using various quasi-3D theories", *J. Sandw. Struct. Mater.*, **18**(1), 3-29. https://doi.org/10.1177/1099636215582217.
Patni, M., Minera, S., Groh, R.M.J., Pirrera, A. and Weaver, P.M. (2018), "Three-dimensional stress analysis for laminated composite and sandwich structures", *Compos. Part B Eng.*, **155**, 299-328. https://doi.org/10.1016/j.compositesb.2018.08.127.
Sahoo, B., Sahoo, B., Sharma, N., Mehar, K. and Panda, S.K. (2020), "Numerical buckling temperature prediction of graded sandwich panel using higher order shear deformation theory under variable temperature loading", *Smart Struct. Syst.*, **26**(5), 641-656. https://doi.org/10.12989/sss.2020.26.5.641.
Shariyat, M. and Alipour, M.M. (2013), "Semi-analytical consistent zigzag-elasticity formulations with implicit layerwise shear correction factors for dynamic stress analysis of sandwich circular plates with FGM layers", *Compos. Part B Eng.*, **49**, 43-64. https://doi.org/10.1016/j.compositesb.2013.01.001.
Shen, H.S. and Li, S.R. (2008), "Postbuckling of sandwich plates with FGM face sheets and temperature-dependent properties", *Compos. Part B Eng.*, **39**, 332-344. https://doi.org/10.1016/j.compositesb.2007.01.004.
Singh, S.J. and Harsha, S.P. (2019), "Exact solution for free vibration and buckling of sandwich S-FGM plates on Pasternak elastic foundation with various boundary conditions", *Int. J. Struct. Stab. Dyn.*, **19**(3), 2019. https://doi.org/10.1142/S0219455419500287.
Sobhy, M. (2016), "An accurate shear deformation theory for vibration and buckling of FGM sandwich plates in hygrothermal environment", *Int. J. Mech. Sci.*, **110**, 62-77. https://doi.org/10.1016/j.ijmecsci.2016.03.003.
Sobhy, M. and Zenkour, A.M. (2019), "Porosity and inhomogeneity effects on the buckling and vibration of double- FGM nanoplates via a quasi-3D refined theory", *Compos. Struct.*, **220**, 289-303. https://doi.org/10.1016/j.compstruct.2019.03.096.
Soleimani-Javid, Z., Amir, S. and Maraghi, Z.M. (2021), "Vibration analysis of sandwich beam with honeycomb core and piezoelectric facesheets affected by PD controller", *Smart Struct. Syst.*, **28**(2), 195-

212. https://doi.org/10.12989/sss.2021.28.2.195.
Thai, H.T., Nguyen, T.K., Vo, T.P. and Lee, J. (2014), "Analysis of functionally graded sandwich plates using a new first-order shear deformation theory", *Eur. J. Mech. A Solids*, **45**, 211-225. https://doi.org/10.1016/j.euromechsol.2013.12.008.
Tounsi, A., Houari, M.S.A., Benyoucef, S. and Adda Bedia, E.A. (2013), "A refined trigonometric shear deformation theory for thermoelastic bending of functionally graded sandwich plates", *Aerosp. Sci. Technol.*, **24**, 209-220. https://doi.org/10.1016/j.ast.2011.11.009.
Trinh, L.C., Vo, T.P., Osofero, A.I. and Lee, J. (2016), "Fundamental frequency analysis of functionally graded sandwich beams based on the state space approach", *Compos. Struct.*, **156**, 263-275. https://doi.org/10.1016/j.compstruct.2015.11.010.
Trinh, L.C., Vo, T.P., Thai, H.T., Nguyen, T.K. and Keerthan, P. (2018), "State-space Levy solution for size-dependent static, free vibration and buckling behaviours of functionally graded sandwich plates", *Compos. Part B Eng.*, **149**, 144-164. https://doi.org/10.1016/j.compositesb.2018.05.017.
Wang, Z.X. and Shen, H.S. (2011), "Nonlinear analysis of sandwich plates with FGM face sheets resting on elastic foundations", *Compos. Struct.*, **93**, 2521-2532. https://doi.org/10.1016/j.compstruct.2011.04.014.
Zenkour, A.M. (2005a), "A comprehensive analysis of functionally graded sandwich plates: Part 1—Deflection and stresses", *Int. J. Solids Struct.*, **42**, 5224-5242. https://doi.org/10.1016/j.ijsolstr.2005.02.015.
Zenkour, A.M. (2005b), "A comprehensive analysis of functionally graded sandwich plates: Part 2—Buckling and free vibration", *Int. J. Solids Struct.*, **42**, 5243-5258. https://doi.org/10.1016/j.ijsolstr.2005.02.016.
Zenkour, A.M. and Aljadani, M.H. (2019), "Porosity effect on thermal buckling behavior of actuated functionally graded piezoelectric nanoplates", *Eur. J. Mech. A Solids.*, **78**, 103835. https://doi.org/10.1016/j.euromechsol.2019.103835.
Zenkour, A.M. and Aljadani, M.H. (2020), "Buckling analysis of actuated functionally graded piezoelectric plates via a quasi-3D refined theory", *Mech. Mater.*, **151**, 103632. https://doi.org/10.1016/j.mechmat.2020.103632.
Zenkour, A.M. and Radwan, A.F. (2020), "Bending and buckling analysis of FGM plates resting on elastic foundations in hygrothermal environment", *Arch. Civil Mech. Eng.*, **20**, 112. https://doi.org/10.1007/s43452-020-00116-z.
Zenkour, A.M. and Radwan, A.F. (2019), "Bending response of FG plates resting on elastic foundations in hygrothermal environment with porosities", *Compos. Struct.*, **213**, 133-143. https://doi.org/10.1016/j.compstruct.2019.01.065.
Zenkour, A.M. and Sobhy, M. (2010), "Thermal buckling of various types of FGM sandwich plates", *Compos. Struct.*, **93**, 93-102. https://doi.org/10.1016/j.compstruct.2010.06.012.
Zhang, R. and Cao, Y. (2022), "Computational mathematical modeling of the nonlinear vibration characteristics of AFG truncated conical nano pipe based on the nonlocal strain gradient theory", *Steel Compos. Struct.*, **42**(5), 599-615. https://doi.org/10.12989/scs.2022.42.5.599.

CC

Appendix

Non-linearity	n	H-Type-A						S-Type-A					
		2-1-2	2-1-1	1-1-1	2-2-1	1-2-1	1-8-1	2-1-2	2-1-1	1-1-1	2-2-1	1-2-1	1-8-1
Yes	0.5	0.0309	0.0314	0.0307	0.0314	0.0311	0.0349	0.0609	0.0634	0.0629	0.0635	0.0644	0.0621
	2	0.0267	0.0284	0.0258	0.0275	0.0263	0.0321	0.0546	0.0579	0.0585	0.0600	0.0626	0.0652
No	0.5	0.0189	0.0195	0.0178	0.0194	0.0192	0.0214	0.0517	0.0542	0.0522	0.0544	0.0571	0.0519
	2	0.0132	0.0141	0.0136	0.0140	0.0139	0.0152	0.0424	0.0448	0.0451	0.0587	0.0492	0.0449

Here, the difference in the values for the non-dimensional critical buckling temperature obtained without considering the non-linear strains is exhibited (Table 3 in Section 3 of the present work). It can be seen that without considering the non-linear strains, the predicted load is lesser than the load obtained using when the non-linearity in the strains is considered.